International Journal of Applied and Natural Sciences
ISSN: 3005-3471
DOI: https://doi.org/10.61424/ijans.v4i1.765
Journal Homepage: https://bluemarkpublishers.com/index.php/IJANS

IJANS
BLUEMARK PUBLISHERS

| RESEARCH ARTICLE

Characterization of Low-Cost Multi-Precursor Ceramic Membranes from Nigerian Agricultural and Biogenic Wastes for Synergistic Removal of Heavy Metals and Azo Dyes from Wastewater

Chukwunonso N. Onyenanu[1] ✉ and Joseph T. Nwabanne[2]
[12]Department of Chemical Engineering, Nnamdi Azikiwe University, Awka, Nigeria
Corresponding Author: Chukwunonso N. Onyenanu, **E-mail**: cn.onyenanu@unizik.edu.ng

| ABSTRACT

The contamination of water resources by heavy metals and recalcitrant azo dyes from textile and industrial effluents remains a critical environmental and public-health challenge, particularly in developing regions. Conventional ceramic membranes, while effective, are often prohibitively expensive due to high-purity raw materials. This study reports the optimized fabrication of a novel low-cost multi-precursor ceramic membrane using abundant, locally sourced Nigerian wastes and natural materials—sawdust, rice husk, snail shell, kaolin clay, and natural clay. Raw materials were pretreated, homogeneously mixed with binders and additives (boric acid, PVA, PEG, CTAB), uniaxially pressed into flat disks (40 mm diameter, 3 mm thickness), and subjected to controlled two-stage sintering. A top-layer coating of fine clay suspension (<2 μm) was applied to enhance selectivity. Comprehensive characterization of both precursors and the final membrane (optimal Sample 25) was performed using EDX, SEM, XRD, FTIR, TG-DTA, XRF, and BET surface-area analysis. The optimized membrane exhibited a high BET surface area of 255.52 m^2/g, a hierarchical micro-mesoporous structure, crystalline phases including quartz, kaolinite, and zeolite, and surface functional groups (Si–O–Si, O–H, C–O) conducive to adsorption and ion exchange. SEM revealed irregular, porous morphologies ideal for high permeability and antifouling, while thermal analysis confirmed structural stability up to sintering temperatures. These properties support synergistic pollutant removal through size exclusion, electrostatic repulsion, adsorption, and Donnan exclusion. The developed membrane, integrated into a custom CAD-designed stainless-steel filtration unit, offers a sustainable, circular-economy approach that valorizes agricultural and biogenic wastes, significantly reduces production costs compared with commercial alumina/zirconia membranes, and aligns with UN Sustainable Development Goals for clean water and sanitation. This work provides a scalable, low-energy fabrication pathway for advanced ceramic membranes tailored for simultaneous heavy-metal and azo-dye remediation in real wastewater matrices.

| KEYWORDS

Low-cost ceramic membranes; multi-precursor; Nigerian waste materials; heavy metal removal; azo dye rejection; wastewater treatment; membrane characterization; sustainable optimization

| ARTICLE INFORMATION

ACCEPTED: 08 February 2026 **PUBLISHED:** 31 March 2026 **DOI:** https://doi.org/10.61424/ijans.v4i1.765

1. Introduction

The increasing contamination of global water sources by industrial effluents, particularly those containing heavy metals and synthetic colors, poses a major risk to public health and the environment. The textile sector is a major source of this pollution, releasing large volumes of wastewater containing hazardous azo dyes and heavy metal complexes that have carcinogenic, mutagenic, and ecotoxicological properties and are resistant to ordinary

degrading processes [Malebadi et al., 2025; Tripathi et al., 2024]. Conventional wastewater treatment methods like coagulation, biological treatment, and adsorption usually fall short of complete removal due to the persistent molecular structures and solubility of these contaminants [Prabhakar et al., 2025; Rakcho et al., 2025; Solaiman et al., 2024]. Therefore, advanced treatment techniques like membrane filtration have gained popularity due to their efficiency in eliminating pollutants through both physical and chemical processes. Because ceramic membranes are more resilient to mechanical, chemical, and thermal stresses than their polymeric counterparts, they are ideal for demanding industrial settings [Jarrar et al., 2024; Wang et al., 2023]. However, the high production costs of conventional ceramic materials (alumina, zirconia) have limited their widespread use [Malebadi et al., 2025; Bensalah et al., 2023].

To overcome this economic obstacle, recent studies have concentrated on the creation of inexpensive ceramic membranes sourced from natural and waste materials, including clays, natural phosphates, coal fly ash, and rice husk ash [Malebadi et al., 2025; Olorunnisola et al., 2025]. These materials not only lower the cost of making things, but they also fit with the ideas of a circular economy by making use of waste from industry and farming. Natural clays such as kaolinite and illite, prevalent in areas like Morocco, have been refined and employed to produce nanofiltration membranes that can eliminate cationic and anionic dyes via size exclusion and electrostatic interactions. [Rakcho et al., 2025; Akoumeh et al., 2025]. Similarly, by utilizing the combined benefits of adsorption and filtration, graphene oxide (GO)-grafted natural phosphate-based substrates have shown significant rejection rates for azo dyes such as Congo Red [Bensalah et al., 2023]. Combining the benefits of each component, such as high surface area, functionalized sites, and customized porosity, could further improve pollutant removal when multiple precursors, such as clay, phosphate, and carbonaceous materials, are integrated into multi-precursor ceramic membranes [Malebadi et al., 2025; Olorunnisola et al., 2025; Onyenanu and Nwabanne, 2025].

To maximize the performance of these membranes, fabrication technique optimization is essential. Ceramic supports are shaped using techniques such as slip casting, tape casting, and extrusion, and porosity, mechanical strength, and permeability are controlled by adjusting sintering temperatures and additives [Olorunnisola et al., 2025]. Advanced modifications that improve interfacial adhesion, selectivity, and antifouling properties include coating with nanomaterials like GO or grafting with silane agents [Bensalah et al., 2023; Kirk et al., 2023]. The interaction processes between dye molecules and membrane surfaces, for instance, have been clarified by density functional theory (DFT) investigations, which show how electrophilic and nucleophilic sites promote adsorption and degradation Additionally, adding photocatalytic materials (TiO_2, ZnO) to clay-based membranes allows for self-cleaning properties and synergistic pollutant breakdown under light irradiation, which decreases fouling and increases lifetime [Olorunnisola et al., 2025; Velusamy et al., 2021].

Membranes with multifunctional removal capabilities are necessary due to the complexity of industrial wastewater, which frequently contains both heavy metals and dyes. If azo dyes are eliminated by size exclusion, electrostatic repulsion, and photocatalytic degradation, heavy metals such as chromium, lead, and cadmium can be adsorbed by ion exchange or complexation with membrane surfaces [Tripathi et al., 2023; Jarrar et al., 2024]. The potential for integrated systems is demonstrated by hybrid processes that have achieved >99% dye removal and a significant reduction in chemical oxygen demand (COD), such as ceramic membrane filtration combined with adsorption using biochar made from vegetable waste [Abhisek, 2025; Santra et al., 2020]. In order to improve scalability and economic feasibility, machine learning (ML) and artificial neural networks (ANNs) are being used more and more to model and optimize these intricate processes. They can forecast operating parameters, fouling behavior, and rejection efficiency [Solaiman et al., 2024; Tayara et al., 2024; Ye, 2025].

Notwithstanding these developments, scaling up inexpensive multi-precursor ceramic membranes for commercial use still presents difficulties. Additional research is necessary to address concerns, including membrane fouling, stability over extended use, and the repeatability of manufacturing techniques [Malebadi et al., 2025; Olorunnisola et al., 2025]. Furthermore, research into recyclable and biodegradable components is necessary due to environmental issues raised by the regeneration and disposal of used membranes [Santra et al., 2020; Abu-Dief et

al., 2025]. In order to improve selectivity and permeability while preserving cost-effectiveness, future research should concentrate on using cutting-edge materials such as metal-organic frameworks (MOFs) and graphene-based composites [Wang et al., 2023; Bensalah et al., 2023]. Commercialization will also depend on the creation of standardized procedures for assessing membrane performance in actual wastewater matrices.

However, the effective creation of low-cost multi-precursor ceramic membranes is a feasible strategy for the simultaneous removal of azo dyes and heavy metals from wastewater [Sandhya et al., 2021]. Through the use of natural and waste materials, advanced modification techniques, and clever process optimization, these membranes can aid in environmentally friendly water management and remediation. This is in line with the UN's Sustainable Development Goals (SDGs) for sanitation and clean water [Solaiman et al., 2024; Jarrar et al., 2024; Sawunyama et al., 2024].

2. Materials and Methods

The process begins with designing and fabricating a membrane wastewater treatment plant, which defines the mechanical layout of the system and provides the foundation for developing a predictive model. This model will estimate plant performance and guide material selection and structural decisions. The next phase involves developing a ceramic membrane, following a structured vertical process. This includes sourcing raw materials, pretreating the materials, characterizing them, producing the membrane, and finally obtaining a finished ceramic membrane. At each stage, the membrane is assessed to ensure it meets the minimum required physical and chemical properties. Once the ceramic membrane is produced, it undergoes optimization, where operational parameters are refined to maximize filtration efficiency and durability. Supporting analytical characterization is conducted concurrently to evaluate the structure, function, and mechanical strength of the membrane. A decision node determines whether the membrane meets the design specifications. If not, the process returns to the optimization stage for further refinement. If it does, the membrane is integrated into the treatment process, beginning with the introduction of raw wastewater, followed by production of treated water, and finally fouling analysis to evaluate membrane degradation. The process ends once treated water is produced within the desired quality limits and fouling analysis has been conducted, completing the treatment cycle.

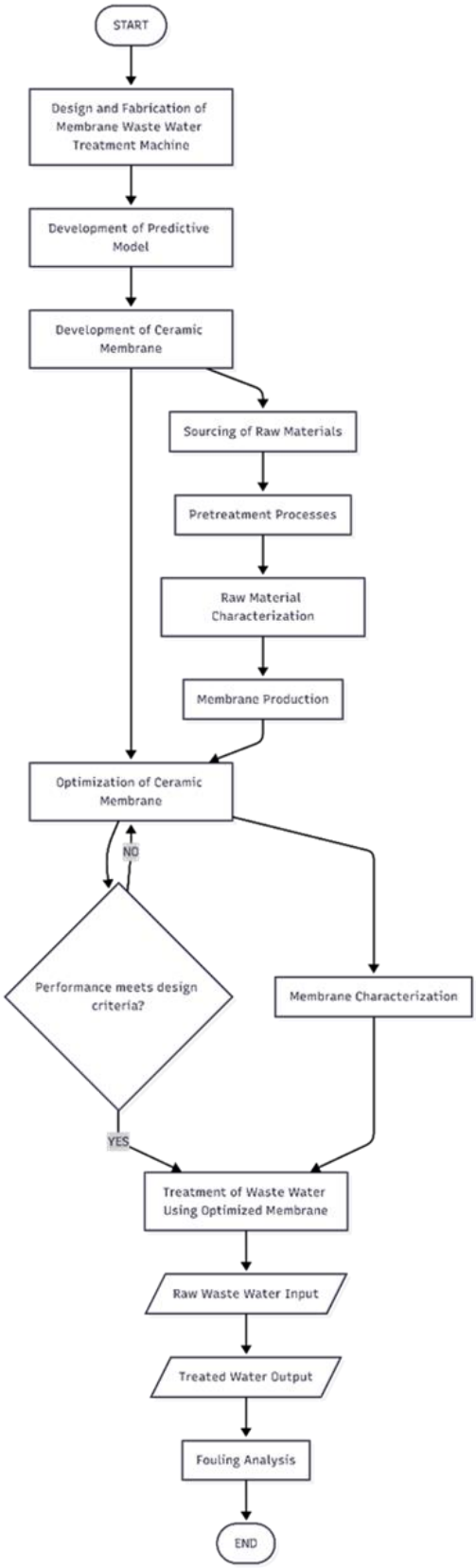

Figure 1: Workflow Diagram of the research work

2.1 Development of Ceramics Membrane

2.1.1 Raw Material Sourcing and Pretreatment

Table 1: Raw Material Sourcing and Pretreatment

S/N	Raw Material	Source/Location	Pretreatment Process	Particle Size	Storage
1	Sawdust	Timber processing site, Eha-Amufu, Enugu State, Nigeria	• Sun-dried for 5 days • Sieved to the desired size	1 mm – 150 µm	Stored in a container
2	Rice Husk	Rice milling site, Eha-Amufu, Enugu State, Nigeria	• Washed with 0.1 M NaOH(aq) under constant stirring for 15 min • Rinsed with deionized water • Oven-dried at 110°C for 6 hrs. • Fired at 1000°C (5°C/min heating rate; 2 hrs. holding time) • Milled and sieved	1 mm – 150 µm	Stored in a container
3	Snail Shell	Head Bridge Market, Onitsha, Anambra State, Nigeria	• Cracked into smaller sizes • Washed with water to remove dirt • Sun-dried for 2 days • Pulverized to powder • Washed with 0.1 M NaOH(aq) • Rinsed with deionized water • Oven-dried at 100°C for 2 hrs.' • Sieved	1 mm – 150 µm	Stored in a container
4	Kaolin Clay	Agu-Awka Sand Mining Site, Awka, Anambra State, Nigeria	• Washing and wet sieving • Filtration • Drying • Milling • Classification	150 µm	Stored in a container
5	Natural Clay	Neke, Enugu State, Nigeria	• Sun-dried for 2 days • Sieved to remove stones • Fired at 1000°C (5°C/min heating rate; 1 hr. holding time) • Ball-milled • Sieved • Suspension in deionized water agitated for 3 hrs. • Natural sedimentation • Fractions < 2 µm recovered and fired at 500°C	• Bulk: 1 mm – 150 µm • Fine fraction: <2 µm (labelled Cn_2)	Stored in separate containers
6	Additives (Soda ash, Boric acid, PVA, CTAB, PEG)	Head Bridge Market, Onitsha, Anambra State, Nigeria	Procured as received	As procured	As received

Figure 2 [a], [b], [c]: Raw material pre-treatment and Membrane production at UNIZIK Chemical Engineering Lab

2.2 Raw Material Characterization

2.2.1 XPS and EDX Analysis

X-ray photoelectron spectroscopy (XPS) and energy dispersive spectroscopy (EDX) analysis were to be performed to determine the elemental composition and chemical binding information on the raw materials.

2.2.2 XRD Analysis

X-ray diffraction spectroscopy (XRD) analysis was to be performed on the raw materials to determine the diffraction pattern, mineralogical composition, and crystalline phases. The XRD analysis is based on passing an X-ray beam through a clay sample. The X-ray defines the structural layers, which are dependent on the d-spacing of the clay minerals. The d-spacing is the exact spacing of the stacking of the crystal lattices, which indicates the arrangement of the atoms in a mineral. The X-ray on passing through the clay samples gives peaks that are typical of each type of diffracted along a group of planes, and the way they are diffracted is characteristic of the arrangement of the atoms within the mineral.

2.2.3 FTIR Analysis

Fourier transform infrared spectroscopy (FT-IR) analysis was performed on all samples isolated to obtain a prompt result regarding the bio-mineral. A few crystals were mixed with KBr (Merck for spectroscopy) and pulverized in an agate mortar to form a homogeneous powder from which, under a pressure of 7 tons, the appropriate pellet was prepared. All spectra were recorded from 4000 to 400 cm-1 using the Perkin-Elmer 3000 MX spectrometer. Scans were 32 per spectrum with a resolution of 4 cm-1. The IR spectra were analysed using the spectroscopic software Win-IR Pro Version 3.0 with a peak sensitivity of 2 cm^{-1}.

2.2.4 SEM analysis

Scanning electron microscopy (SEM) analysis was to be performed to determine the morphological characteristics (surface structures) of the raw materials. All samples must be of an appropriate size to fit in the specimen chamber and are generally mounted rigidly on a specimen holder called a specimen stub. Several models of SEM can examine any part of a 6-inch (15 cm) semiconductor wafer, and some can tilt an object of that size to 450. Samples are coated with a platinum coating of electrically conducting material, deposited on the sample either by low-vacuum sputter coating or by high-vacuum evaporation. SEM instruments place the specimen in a relatively high-pressure chamber where the working distance is short, and the electron optical column is differentially pumped to

keep the vacuum adequately low at the electron gun. The high-pressure region around the sample in the ESEM neutralizes charge and provides an amplification of the secondary electron signal. Low-voltage SEM is typically conducted in an FEG-SEM because the field emission guns (FEG) are capable of producing high primary electron brightness and small spot size even at low accelerating potentials.

2.2.5 TG-DTA Method

The changes in physical and chemical properties of the raw materials due to an increase in temperature were to be measured using a thermogravimetric and differential thermal analysis (TG-DTA).

2.3 Fabrication of Membrane

2.3.1 Membrane production procedure

Predetermined mass of the treated clay, rice husk ash, kaolin, sawdust, and snail shell particles were to be thoroughly mixed using a mortar for 30 minutes to obtain a homogeneous mixture. An appropriate amount of boric acid, PVA, and/or PEG (1-5 wt%) was to be added as a binding agent, followed by the addition of deionized water to form a paste. And thereafter, a stipulated mass of the paste is weighed (in order to maintain constant membrane thickness) and cast into a cylindrical mold. The paste was to be compacted under 150 MPa in the cylindrical mold, forming flat disks with a diameter of 40 mm and a thickness of 3 mm, in a hydraulic press for 30 minutes. After which it is removed and left to air-dry at room temperature for 24 hrs.

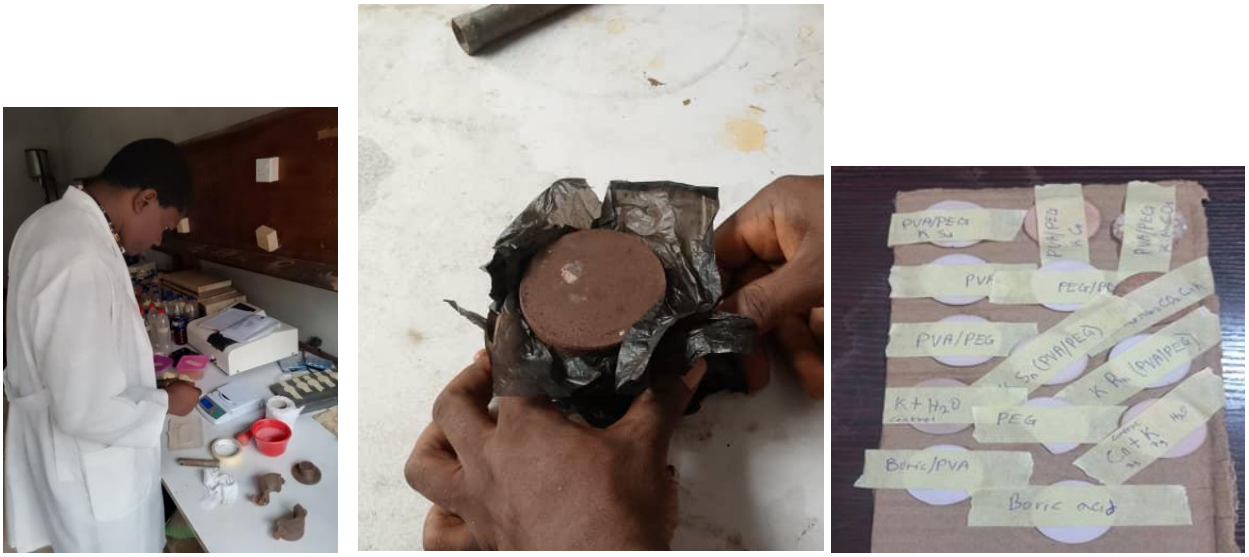

Figure 3 [a], [b], [c]: Membrane production at UNIZIK Chemical Engineering Lab

2.3.2 Sintering of Membrane Support

All the obtained flat compacts were to be sintered at a heating rate of 5 °C min^{-1} according to the following program stages:

1. 2hrs annealing at 250 °C to remove absorbed and constitutional water,
2. 1h annealing at 500 °C to degrade organic phases,
3. 1h annealing at 750 °C to achieve complete decomposition of binders (PVA and PEG) and clay mineral dehydroxylation,
4. 2hrs annealing at 1000 °C for recrystallization.

Figure 4 [a], [b]: Sintering of the membrane at the muffler furnace.

2.3.3 Membrane Top Layer

Clay (Cn_2) suspension was prepared by stirring a mixture of Cn_2 (4 wt%; ≤2 µm), distilled water containing 0.05 g of CTAB (66 wt%), and 12 wt% aqueous PVA (30 wt%) for 2 hours at 250 rpm and allowed to stand for 4 hours. The suspension (10 ml) was to be drop-cast on the support, and excess fluid was removed using a casting knife edge, thus reducing the thickness of the deposited film layer. The liquid phase is to be evaporated, and the membrane dried for 24 h at 80 °C. The same procedure is to be followed when soda ash, kaolin, and Cn_2 are to be utilized, but soda ash and kaolin are to be prepared separately.

2.3.4 Sintering of the Membrane Layer

Membrane layer sintering was performed by annealing at 300 °C for 2 hrs. to completely decompose PVA, followed by further annealing at 1000 °C for 2 hrs. To ensure no formation of cracks, a heating rate of 1 °C min^{-1} was to be used.

2.4 Summary of Instrumental Characterization of the Produced Membrane

Table 2: Instrumental Characterization of the Produced Membrane

S/N	Analytical Technique	Purpose / Parameters Evaluated	Method / Procedure	Key Outputs / Calculations
1	**TG-DTA** (Thermogravimetric Analysis – Differential Thermal Analysis)	Structural evolution and thermal properties of the fabricated ceramic membrane	Heating sample under controlled atmosphere while measuring weight change (TG) and heat flow (DTA)	Thermal stability, decomposition temperatures, phase transitions, and mass loss profiles
2	**XRD** (X-ray Diffraction)	Evaluation of phase transformations and precursor states within the membrane structural matrix	X-ray beam directed at crystalline sample; analysis of diffraction pattern (2θ vs. intensity)	Crystalline phase identification, mineralogical composition, and degree of crystallinity
3	**SEM** (Scanning Electron Microscopy)	Morphological characterization of membrane surface and cross-section	Electron beam scanning; high-resolution imaging at various magnifications	Surface topography, pore structure, layer thickness, and defect detection
4	**FESEM** (Field Emission Scanning Electron Microscopy)	Verification of microstructures of the fabricated ceramic membrane	High-resolution electron microscopy with a field emission gun	Ultra-high-resolution surface morphology, fine structural details, and grain structure
5	**EDX** (Energy Dispersive X-ray Spectroscopy)	Investigation of the chemical/elemental composition of the ceramic membrane	X-ray emission analysis coupled with SEM	Elemental composition (wt%, at%), elemental mapping, impurity detection
6	**BET** (Brunauer–Emmett–Teller)	Determination of specific surface area, pore volume, and pore size distribution	Nitrogen adsorption/desorption isotherms at 77 K	Surface area (m^2/g), pore volume (cm^3/g), average pore diameter (nm), pore size distribution
7	**FTIR** (Fourier Transform Infrared Spectroscopy)	Identification of surface functional groups and chemical bonds	Infrared radiation absorption; KBr pellet method (4000–400 cm^{-1})	Functional group identification (O–H, Si–O, Al–O, C=O, etc.), chemical bonding, and adsorptive properties

2.5 Final CAD Diagram of the Waste Water Treatment Machine

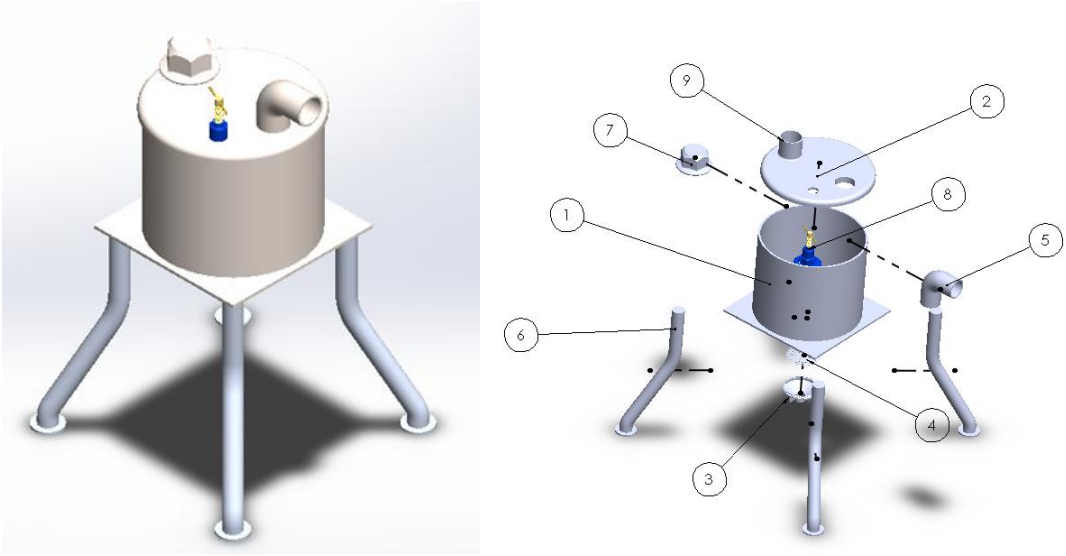

Figure 5 [a], [b]: 3D CAD diagram and Exploded view of the water treatment machine

The wastewater treatment machine [Onyenanu et al., 2025], designed to utilize a ceramic membrane synthesized from local precursors, operates by filtering wastewater containing lead (II) ions, cadmium (II) ions, Disperse Yellow 7, and Trypan Blue dyes through a series of precisely engineered components labeled as follows: (1) the cylindrical body, a 10-liter AISI 316L stainless steel chamber housing the ceramic membrane where filtration occurs; (2) the top cover with water inlet, also stainless steel, allowing contaminated wastewater to enter the system; (3) the base plate, a perforated AISI 316 stainless steel sheet supporting the membrane and facilitating permeate drainage; (6) four support legs, made of 6061 aluminum alloy, elevating the cylindrical body for stability and access; (5) the pressure inlet pipe, an elbow-shaped AISI 316 stainless steel conduit directing filtered water outflow; (4) the sieve, a stainless steel component integrated with the support legs to pre-filter larger particles; (7) the wastewater cap/plug, an alloy steel seal for maintenance access; (8) the pressure regulator, to be stainless steel, controlling transmembrane pressure to optimize flux and retention; and (9) the wastewater inlet enables wastewater in the system for treatment. The working principle involves wastewater entering through the top cover's inlet, passing through the sieve for preliminary filtration, and then being forced through the ceramic membrane within the cylindrical body under regulated pressure, where size exclusion, adsorption, and Donnan exclusion mechanisms remove heavy metals and dyes. The filtered permeate exits via the pressure inlet pipe, while retentate is managed through the base plate's perforations, ensuring efficient treatment and compliance with environmental standards.

3. Results and Discussion

3.1 Results from Raw Material Characterization.

3.1.1 Elemental Composition Analysis Using Energy Dispersive X-ray Spectroscopy (EDX)

Energy Dispersive X-ray Spectroscopy (EDS/EDX), a method used to determine the elemental composition of materials by examining the X-rays generated from a sample when attacked with an electron beam, is the subject of this paper. Complete elemental composition tables for all precursors are compiled in Appendix B.1, showing weight percentages and atomic ratios. It concentrates on the material characterization of a ceramic membrane. This technique is essential for comprehending the chemical composition of the wastewater treatment-specific ceramic membrane. In ceramic materials made of clay, kaolin, snail shell, sawdust, rice husk ash, and soda ash, EDS/EDX offers information on the presence and distribution of elements, including silicon, aluminum, oxygen, and others. By mapping the elemental composition, this technique helps verify the incorporation of these raw materials and their impact on the membrane's properties, such as Permeation Flux, Flexural Strength, Porosity, and Pore Size.

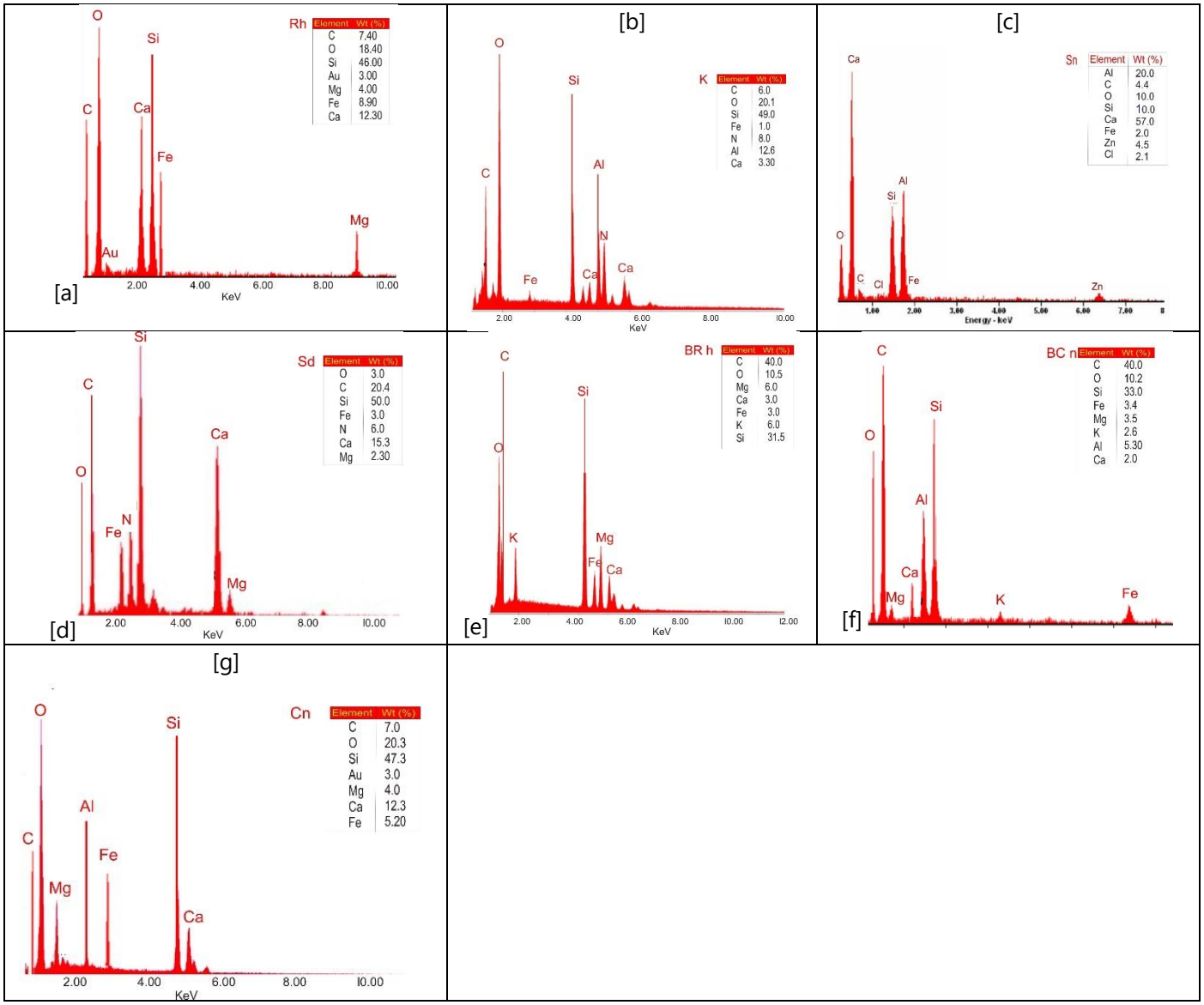

Figure 6: Scanning Electron Microscopy (SEM) micrographs of ceramic membrane precursors at various magnifications. (a) Raw rice husk (Rh), (b) Kaolin/kolin (K), (c) Snail shell (Sn), (d) Sawdust (Sd), (e) Burnt rice husk (BRh), (f) Burnt clay (BCn), (g) Raw clay (Cn).

3.1.2 Discussion of the Elemental Composition Analysis of Membrane Percusors

The EDS analysis of Kolin (K) shows Silicon (Si) as the most abundant element at 49.0 Wt%, with Oxygen (O) also present in high amounts at 20.1 Wt%. Aluminum (Al) is a notable component at 12.6 wt%, which aligns with the typical composition of kaolin clay. Carbon (C) accounts for 6.0 Wt%, while Nitrogen (N) is present at 8.0 Wt%. Minor constituents include Calcium (Ca) at 3.30 Wt% and Iron (Fe) at 1.0 Wt%. The strong Si and Al peaks confirm the aluminosilicate nature of Kolin. The EDS spectrum for Snail Shell (Sn) indicates an overwhelmingly high concentration of Calcium (Ca) at 57.0 Wt%, which is expected given that snail shells are primarily composed of calcium carbonate. Aluminum (Al) is also significantly present at 20.0 Wt%, and Silicon (Si) at 10.0 Wt%. Oxygen (O) is found at 10.0 Wt%, and Carbon (C) at 4.4 Wt%. Minor elements include Zinc (Zn) at 4.5 Wt%, Chlorine (Cl) at 2.1 Wt%, and Iron (Fe) at 2.0 Wt%. The dominance of calcium highlights its role as the main structural component. Sawdust (Sd) analysis reveals Silicon (Si) as the most abundant element at 50.0 Wt%, suggesting mineral contamination or significant silica content in the original wood. Carbon (C) is present at 20.4 Wt%, and Calcium (Ca) at 15.3 Wt%. Nitrogen (N) and Iron (Fe) are found at 6.0 wt% and 3.0 wt%, respectively. Oxygen (O) content is

relatively low at 3.0 Wt%, and Magnesium (Mg) is at 2.30 Wt%. The high silicon content is a key characteristic of this sample. The EDS spectrum for Burnt Rice Husk (BR h) shows high Carbon (C) at 40.0 Wt%, indicating incomplete combustion or residual carbonaceous material. Silicon (Si) is also substantial at 31.5 wt%, expected given the high silica content of raw rice husk. Oxygen (O) is at 10.5 Wt%. Other elements include Potassium (K) and Magnesium (Mg), both at 6.0 Wt%, and Iron (Fe) and Calcium (Ca), both at 3.0 Wt%. The significant silicon and carbon presence highlight this material as silica-rich ash with residual carbon. Burnt Clay (BC n) analysis shows Carbon (C) as the most abundant element at 40.0 Wt%, possibly indicating organic matter or incomplete burning. Silicon (Si) is also a major component at 33.0 wt%, typical for clay minerals. Oxygen (O) is at 10.2 Wt%, and Aluminum (Al) is at 5.30 Wt%. Other detected elements include Iron (Fe) at 3.4 Wt%, Magnesium (Mg) at 3.5 Wt%, Potassium (K) at 2.6 Wt%, and Calcium (Ca) at 2.0 Wt%. The silicon and aluminum presence confirms the aluminosilicate nature of clay. The EDS spectrum for Clay (Cn) shows Silicon (Si) as predominant at 47.3 Wt%, followed by Oxygen (O) at 20.3 Wt%, and Calcium (Ca) at 12.3 Wt%. Carbon (C) is present at 7.0 Wt%. Minor elements include Iron (Fe) at 5.20 Wt%, Aluminum (Al) at 4.0 Wt%, and Magnesium (Mg) at 4.0 Wt%. Gold (Au) is also detected at 3.0 Wt%. The high silicon and oxygen content, along with aluminum, are characteristic of clay minerals.

These values are consistent with explanations on natural or altered aluminosilicates, as well as zeolite-kaolin-quartz composites, materials sourced from kaolin and rice husk ash/clay blends for economical ceramic membranes. Typical BET surface areas of natural clays/zeolites are typically 200–400 m^2/g (e.g., kaolin-based zeolite 4A from Nigerian materials with increased porosity post-treatment) [Mgbemere et al., 2019], geopolymer-zeolite composites (13–400 m^2/g based on the degree of activation) [Obada et al., 2017]. From clays and rice husk in particular deposits, hierarchical mesoporous materials yield Type IV isotherms with an H3/H4 hysteresis reminiscent of slit-shaped pores and interparticle voids [Schackow et al., 2020]. Pore volumes ~0.45–0.60 cm^3/g and pore sizes ~2–3 nm is similar to those in inexpensive ceramic precursors from Nigerian clay/kaolin/rice husk, where organics promote pores and Si/Al/Ca form framework porosity [Ihekweme et al., 2020]. The higher surface area and smaller pores of Sample 35 imply better optimization (for instance, lighter activation or less quartz doping), leading to greater adsorption/filtration capabilities relative to Sample 25.

3.1.3 Surface Morphology and Microstructure Examination via Scanning Electron Microscopy (SEM)

This section presents a detailed analysis of the morphology of various materials, including snail shell (Sn), kolin (K), sawdust (Sd), burnt rice husk (BR h), raw rice husk (Rh), burnt clay (Bcn), and raw clay (Cn), as observed through Scanning Electron Microscopy (SEM). Each image provides insights into the surface characteristics, particle shape, and overall microstructure of these materials, which are crucial for understanding their physical properties and potential applications. The varying magnifications and scales in the images highlight different levels of detail, from the rough, irregular surfaces of some materials to the more defined crystalline or fibrous structures of others.

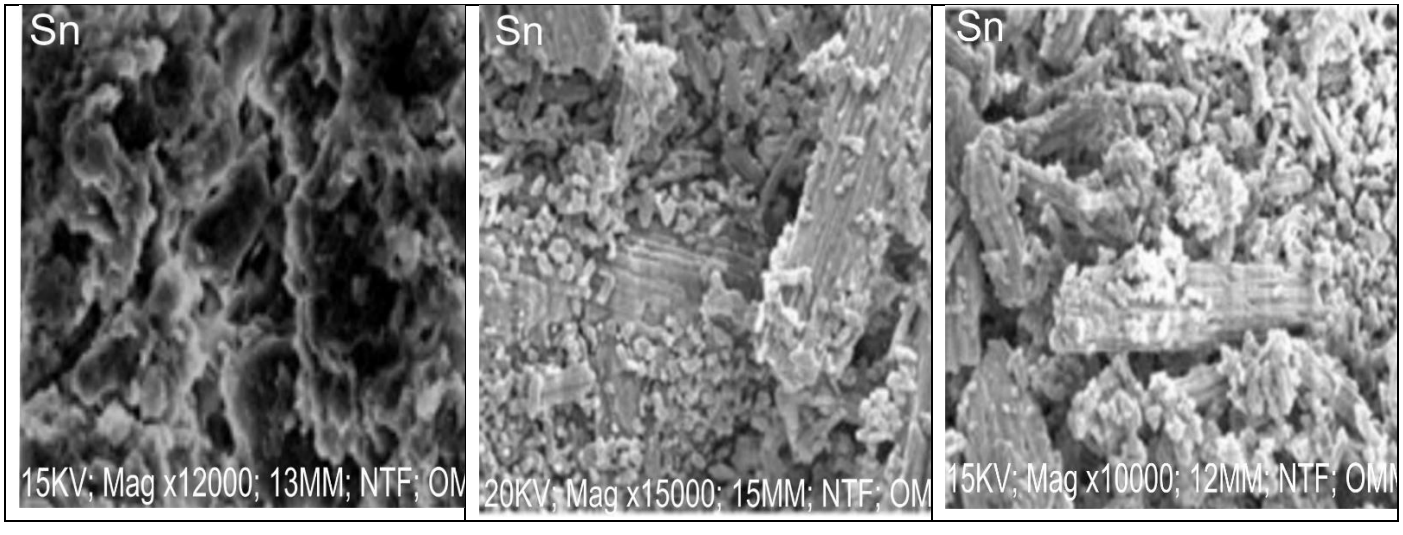

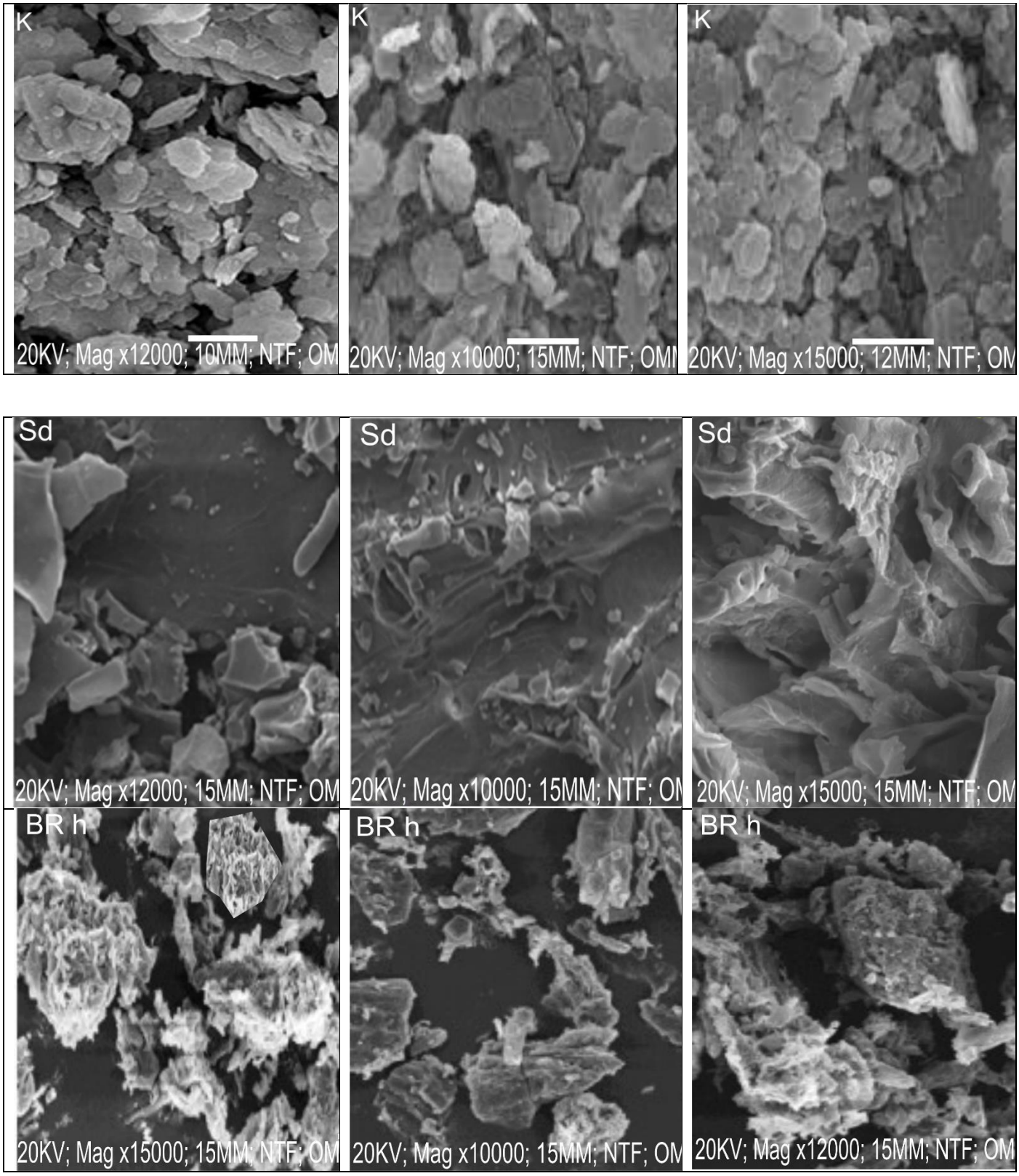
K
20KV; Mag x12000; 10MM; NTF; OM
K
20KV; Mag x10000; 15MM; NTF; OMI
K
20KV; Mag x15000; 12MM; NTF; OM
Sd
20KV; Mag x12000; 15MM; NTF; OM
Sd
20KV; Mag x10000; 15MM; NTF; OM
Sd
20KV; Mag x15000; 15MM; NTF; OM
BR h
20KV; Mag x15000; 15MM; NTF; OM
BR h
20KV; Mag x10000; 15MM; NTF; OM
BR h
20KV; Mag x12000; 15MM; NTF; OM

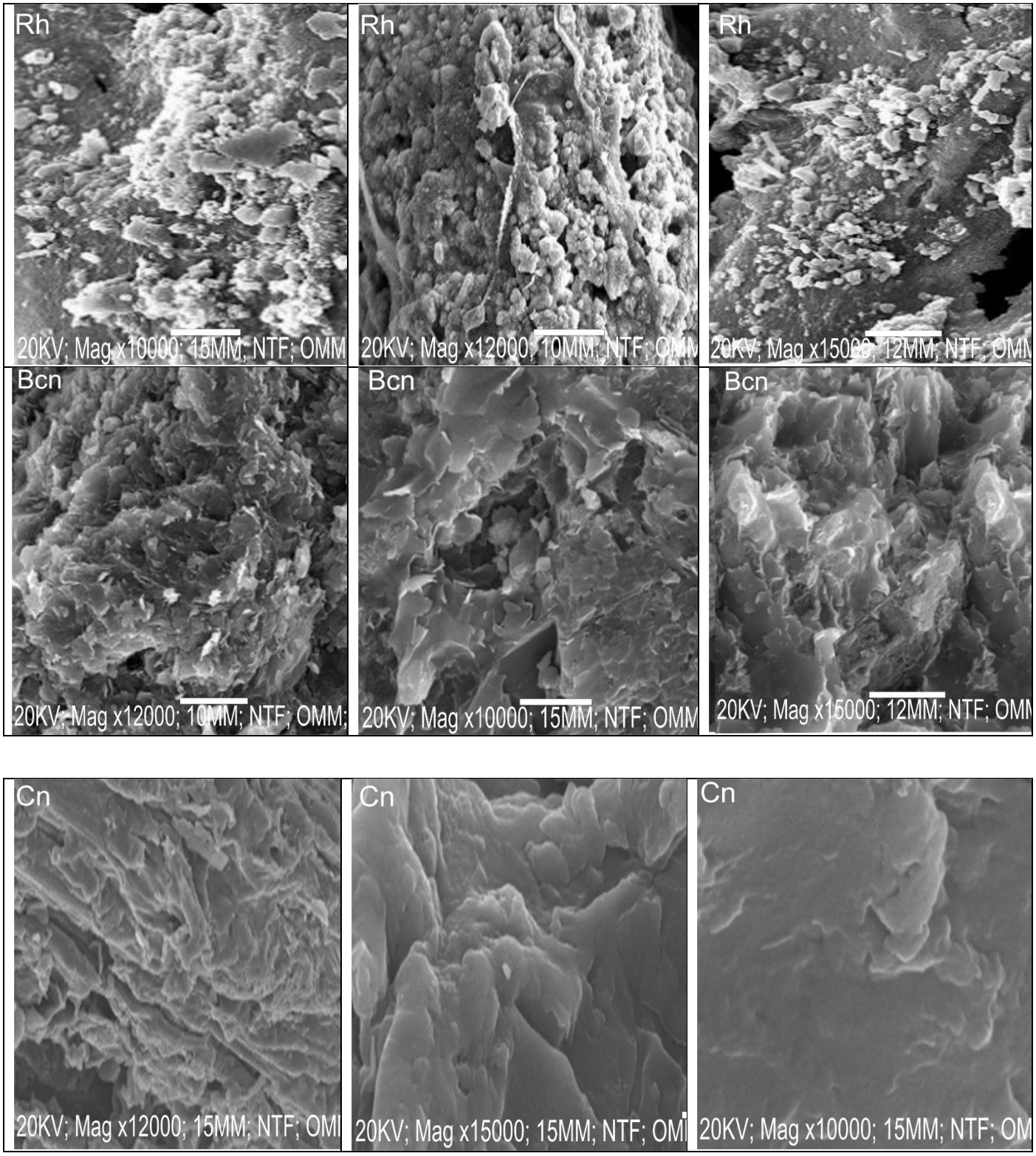

Figure 7: Scanning Electron Microscopy (SEM) micrographs of ceramic membrane precursors. High-resolution images at 15–20 kV and magnifications of ×10,000 to ×15,000 (scale bars 20–200 μm) showing surface morphology and microstructure: [a–c] Snail shell (Sn); [d–f] Kolin/kaolin (K); [g–i] Sawdust (Sd); [j–l] Burnt rice husk (BRh); [m–o] Raw rice husk (Rh); [p–r] Burnt clay (BCn); [s–u] Raw clay (Cn).

3.1.4 Discussion of the Surface Morphology and Microstructural Examination of the Membrane Percusors

The SEM images of Snail Shell (Sn) reveal a highly irregular and porous surface morphology across three magnifications. Figure 7[a], captured at 15KV with x12000 magnification and a 50µm scale bar, displays a rough, rocky texture with numerous interconnected pores and irregularly shaped particles. This morphology aligns with the calcium carbonate composition of biological shells, exhibiting complex layered structures that provide strength and lightweight properties. The presence of voids and particle size variations suggests potential for high surface area applications. Figure 7[b], taken at 20KV with x15000 magnification and a 20µm scale bar, reveals a mixture of elongated fibrous structures alongside granular irregular particles. The higher magnification provides greater detail, with fibrous characteristics potentially indicating organic remnants or specific crystalline arrangements within the shell structure. This varied morphology highlights the heterogeneous nature of this biological material, resulting from complex growth patterns. The final image, captured at 15KV with x10000 magnification and a 100µm scale bar, reinforces the highly irregular and rough surface composed of interconnected particles and robust structural fragments. Both granular and elongated features remain evident across all images, confirming the consistent heterogeneity in particle sizes and shapes. The open, porous structure observed throughout demonstrates the material's intricate internal network, supporting its potential for applications requiring high surface area or specific mechanical properties derived from its complex morphology. This aligns with literature on snail shells as primarily aragonitic $CaCO_3$, exhibiting complex layered or cross-lamellar arrangements with voids for strength and lightness [Parveen et al., 2020; Podaralla et al., 2024]. SEM studies confirm heterogeneous, porous surfaces with crystalline fragments, often species-specific, supporting its use as a Ca-flux or pore-modifier in ceramics.

The SEM images of Kolin (K) reveal a distinct lamellar or plate-like morphology characteristic of kaolin clay minerals across three magnifications. Figure 7[c], captured at 20KV with x12000 magnification and a 150µm scale bar, shows stacked or aggregated particles forming layered structures that extend over relatively large areas. This platy morphology directly corresponds to the crystal structure of kaolinite, consisting of stacked silicate layers, which provides high surface area and adsorptive capabilities valuable in ceramics, paper, and cosmetics applications. Figure 7[d], taken at 20KV with x10000 magnification and a 200µm scale bar, confirms the lamellar structure with a broader view. The individual platelets appear somewhat less distinct due to slight aggregation, yet the overall platy characteristic remains evident. The material presents as randomly oriented flakes and aggregates, typical of powdered or processed clay, reinforcing its identity as a well-defined layered silicate mineral. Figure 7[e], captured at 20KV with x15000 magnification and a 50µm scale bar, provides a closer examination of particle distribution, showing larger, defined plate-like particles alongside smaller, irregular aggregates. The dispersed particles overlap in some areas, forming a relatively dense structure. The finer details reveal inter-particle voids and surface roughness, important factors for applications as fillers, adsorbents, or composite components. The consistency across all three images confirms the material's predominant layered morphology. This is consistent with numerous SEM/AFM analyses of kaolinite, illustrating that plates are 200–500 nm pseudohexagonal in shape and can be stacked in books or at random angles, and that high surface area arises from inter-particle voids [Yang et al., 2023]. This structural feature makes them effective plasticizers and adsorbents in membrane preparation.

The SEM images of Sawdust (Sd) reveal a heterogeneous morphology characterized by large, irregular fragments and elongated fibrous structures across three magnifications. Figure 7[f], captured at 20KV with x12000 magnification and a 100µm scale bar, displays angular shapes and fractured surfaces indicating mechanical processing of wood. The presence of both larger fragments and smaller irregular particles confirms the heterogeneous nature typical of sawdust, with exposed cellular structures influencing water absorption and mechanical strength. Figure 7[g], taken at 20KV with x10000 magnification and a 50µm scale bar, provides a closer examination of surface details, revealing compacted and fragmented areas with plant cell wall remnants alongside amorphous regions. This irregular porous morphology contributes to absorbency and packing density, important for applications in biomass fuel, animal bedding, or composite materials. Figure 7[h], captured at 20KV with x15000 magnification and a 100µm scale bar, highlights elongated intertwined fibers and irregular fractured fragments with rough porous surfaces consistent with wood's fibrous nature. This image emphasizes the heterogeneous composition containing various cellular components and milling debris. The intricate fiber-particle network observed is critical for understanding bulk properties, including thermal conductivity and mechanical behavior,

when incorporated into other materials. This agrees with the findings of wood dust SEM with conical/rectangular/cylindrical particles (2–70 μm) with some exposed cell remnants and some variability due to milling [Yepes et al., 2011]. The heterogeneous fibrous structure acts as a pore former by burnout during sintering. The SEM images of Burnt Rice Husk (BR h) reveal a highly porous and irregular morphology characteristic of charred biomass material across three magnifications. Figure 7[i], captured at 20KV with x15000 magnification and a 100μm scale bar, displays fragmented particles with remnants of the original cellular structure of rice husk, though significantly modified by combustion. An embedded smaller image offers a detailed view of a particularly rough cellular structure. This porous and fragmented nature suggests high surface area, making it potentially suitable as an adsorbent, pozzolanic material in cement, or catalyst support. Figure 7[j], taken at 20KV with x10000 magnification and a 50μm scale bar, shows a more dispersed collection of irregular angular particles. Many particles exhibit sharp edges and fragmented appearances, indicating a brittle nature after burning. The absence of a continuous, well-defined structure confirms significant transformation during combustion, with the breakdown of the original organic matrix. This morphology is important for understanding handling, grinding, and reactivity in various applications. Figure 7[k], captured at 20KV with x12000 magnification and a 100μm scale bar, showcases a combination of larger intact fragments alongside smaller granular particles. The surfaces appear rough and textured, with some exhibiting residual cellular patterns. This image emphasizes the morphological heterogeneity of burnt rice husk, which varies depending on combustion extent and conditions. The variations in particle size and surface characteristics are important factors for composite materials or additives, where particle packing and interaction play significant roles. The consistent porous architecture across all images confirms the material's potential for high surface area applications. The results of numerous investigations on RHA verify porous, honeycombed/interstitial (10 μm honeycombed + <50 nm interstitial pores) structures with high surface area after burning, and it is frequently paired due to silanol/hydroxyl bonding [Xu et al., 2012; Jonathan et al., 2020; Thiedeitz et al., 2020]. This justifies its function in increasing the porosity of the membrane.

The SEM images of Rice Husk (Rh) reveal a highly textured and rough surface morphology across three magnifications. Figure 7[l], captured at 20KV with x10000 magnification and a 200μm scale bar, displays a collection of irregularly shaped particles, with some appearing elongated and fibrous while others are more granular. This morphology aligns with the natural silica-rich structure of rice husk, which possesses a complex cellular arrangement. The surface roughness and diverse particle shapes are key characteristics influencing its physical and chemical interactions in various applications. Figure 7[m], taken at 20KV with x12000 magnification and a 150μm scale bar, provides a detailed view of the rough and porous surface, revealing an interconnected network of particles and voids. This inherent porosity, attributed to its cellular structure, contributes to lightweight properties and high surface area, making rice husk suitable for adsorbents, insulation materials, or composite fillers. The visible particle network suggests potential for fluid absorption and mechanical interlocking. Figure 7[n], captured at 20KV with x15000 magnification and a 50μm scale bar, distinctly shows smaller rod-like or elongated particles interspersed among larger irregular fragments. The rough texture with visible pores and crevices emphasizes the heterogeneous nature of rice husk, composed of both fine particles and coarser elements. These diverse morphologies contribute to its unique physical properties, including abrasive nature and utility as a lightweight aggregate or silica source. This reflects a natural lignocellulosic silica-rich structure with interconnected voids, as seen in RHA precursor studies [Mohamed Ariff et al., 2022].

The SEM images of Burnt Clay (BCn) reveal irregularly shaped compacted aggregates across three magnifications. Figure 7[o], captured at 20KV with x12000 magnification and a 150μm scale bar, shows a mixture of larger plate-like structures and finer granular particles with relatively rough surfaces. Some areas exhibit evidence of sintering or partial melting from the burning process, which has altered the original clay structure to form a more consolidated material. This morphology is important for understanding mechanical and thermal properties in construction applications. Figure 7[p], taken at 20KV with x10000 magnification and a 200μm scale bar, offers a broader perspective, highlighting particle aggregation with both larger and smaller irregular fragments. Some areas appear densely packed while others show visible inter-particle voids. The rough, fragmented texture reflects high-temperature treatment, with variations in particle size and aggregation relevant for applications where packing

density and surface area are critical. Figure 7[q], captured at 20KV with x15000 magnification and a 50µm scale bar, provides detailed surface features revealing highly irregular, fragmented morphology. Particles appear tightly packed in some regions, forming denser structures, while other areas show defined individual particles with rough surfaces. This microstructure indicates transformation during burning, leading to new phase formation and material consolidation. The intricate particle surfaces and inter-particle contacts are essential for understanding material strength and durability.

The SEM images of Clay (Cn) reveal stacked or layered structures characteristic of clay minerals across three magnifications. Figure 7[r], captured at 20KV with x12000 magnification and a 100µm scale bar, shows individual particles as flakes or plates that are often aggregated. The surface appears relatively smooth compared to other materials, though some irregularities and small crevices are visible. This platy morphology is a defining feature influencing plasticity and water retention properties, with layer arrangement and aggregation degree crucial for applications in ceramics, brickmaking, and as a binder. Figure 7[s], taken at 20KV with x15000 magnification and a 100µm scale bar, offers a detailed view emphasizing the layered structure with visible individual clay platelets. The particles appear closely packed, forming a relatively dense material. Some areas show an amorphous or cohesive appearance, suggesting potential for particle interlocking. The smooth surface in many regions is consistent with the fine particulate nature of clay, with this morphology fundamental to understanding engineering properties such as shear strength and compressibility. Figure 7[t], captured at 20KV with x10000 magnification and a 50µm scale bar, provides a close-up showing a relatively smooth continuous texture with minor undulations. The layered structure remains evident, though less pronounced, possibly due to viewing angle or sample preparation. The fine-grained nature is clear, with tightly packed particles forming a cohesive mass. This consistent, relatively uniform morphology is essential for clay's widespread use in construction, pottery, and various industrial products. Clay SEM images of burnt and raw clay generally reveal aggregation, partial vitrification, and densification in the fired forms when compared to the loose, platy morphology of raw clay, which affects strength and porosity [Schackow et al., 2020; Boussemghoune et al., 2020]. These are consistent with Nigerian clay precursors for ceramics, in which burning compacts particles for resilient matrices.

3.1.5 Results of the Crystallographic Phase Identification by X-ray Diffraction (XRD)

This section delves into the crystallographic analysis of various materials using X-ray Diffraction (XRD). XRD is a powerful, non-destructive technique that reveals the atomic and molecular structure of crystalline materials. When X-rays interact with a crystalline sample, they are diffracted at specific angles determined by the arrangement of atoms in the crystal lattice. The resulting diffraction pattern, typically plotted as intensity versus the diffraction angle 2θ, provides a unique fingerprint for identifying the crystalline phases present in a material. Each peak in the diffractogram corresponds to a specific crystal plane and can be matched against databases of known crystalline structures to identify minerals and compounds. This technique is essential for understanding the phase composition, crystallinity, and structural changes within materials, which directly influence their physical and chemical properties.

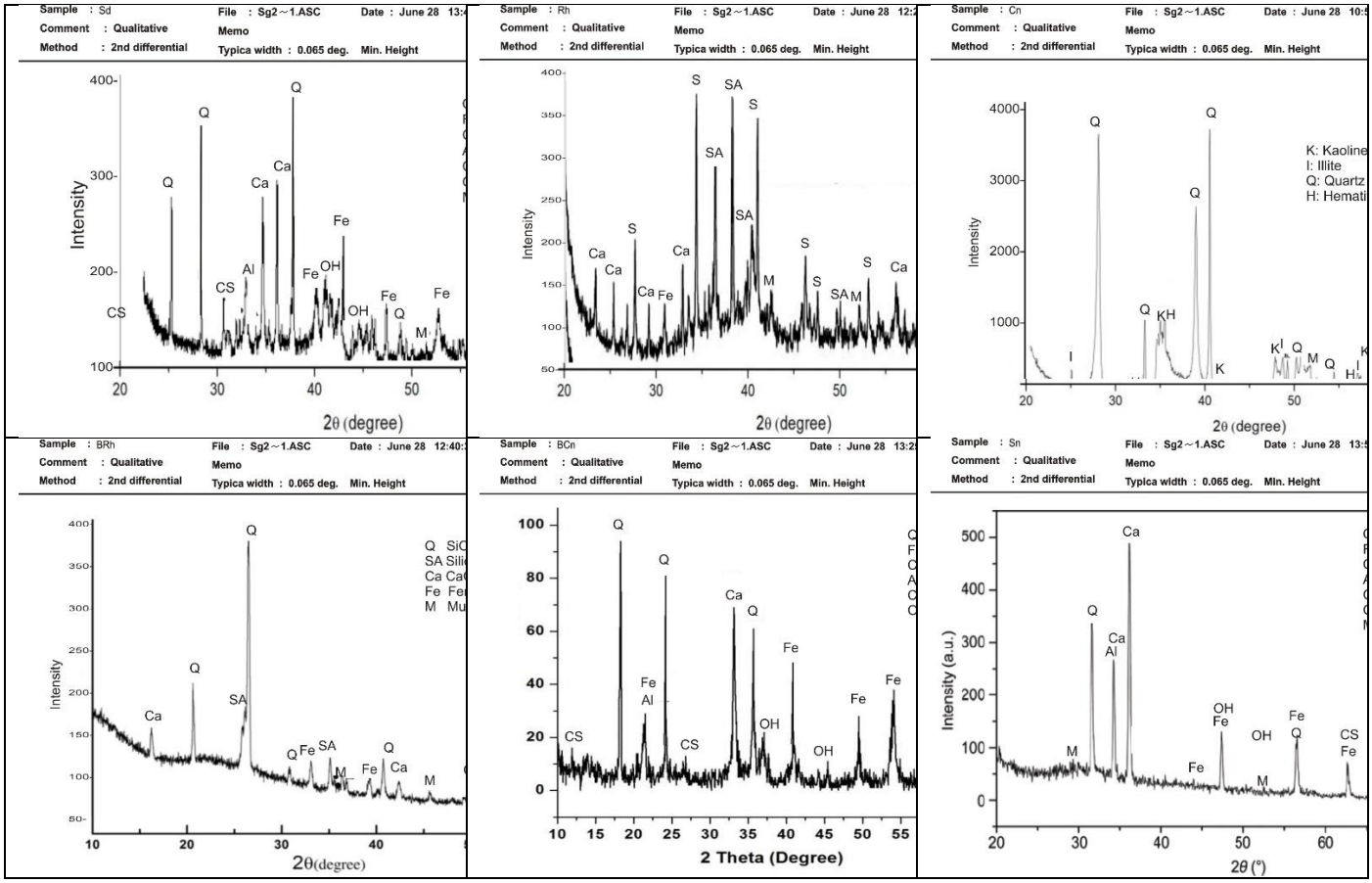

Figure 8: X-ray Diffraction (XRD) patterns of ceramic membrane precursors. (a): Sawdust (Sd), (b): Rice Husk (Rh), (c): Clay (Cn), (d): Burnt Rice Husk (BRh), (e): Burnt Clay (BCn), (f): Snail Shell (Sn).

3.1.6 Discussion of the Results of the Crystallographic Phase Identification by X-ray Diffraction (XRD) for the Membrane Percusors

The X-ray Diffraction patterns reveal distinct crystalline phases across all samples. For Sawdust (Sd) in Figure 4.10[a], prominent Quartz (SiO_2) peaks indicate crystalline silica as a major component. Other identified phases include Iron Oxide (Fe_2O_3), Calcium Carbonate ($CaCO_3$), Aluminum Silicate ($AlSiO_4$), Calcium Silicate (Ca_2SiO_4), Aluminum Hydroxide (Al (OH)), and Muscovite. This complex composition suggests mineral inclusions within the wood structure or environmental contamination. Literature confirms quartz and minor silicates in sawdust due to environmental/processing impurities, with XRD often detecting quartz, feldspars, and clay traces in wood dust for composites or membranes (Marques et al., 2025; Jannat et al., 2021). High quartz intensity aligns with contamination, enhancing silica content for membrane stability. Rice Husk (Rh) in Figure 4.10[b] shows distinct crystalline silica peaks (SiO_2) as the dominant phase. Additional phases include Silica-Aluminate, Calcium Oxide (CaO), Ferrite, and Mullite, indicating a complex inorganic composition beyond expected amorphous silica. The high intensity of silica peaks confirms substantial crystalline silica presence. Studies report raw RH with minor quartz, while burning induces cristobalite/quartz/mullite (Hossain et al., 2018; Serra et al., 2016). The observed crystalline silica suggests some pre-processing or natural variation. Clay (Cn) in Figure 4.10[c] exhibits characteristic peaks of clay minerals, with Quartz (SiO_2) as the most intense phase. Other identified minerals include Kaoline, Illite, and Hematite. The presence of Kaoline and Illite confirms the aluminosilicate composition typical of natural clay, with well-crystallized quartz structure indicated by sharp intense peaks. This is consistent with Nigerian clays/kaolins, which are dominated by kaolinite (peaks ~12.3°, 20°, 25° 2θ for the first three orders of diffraction), quartz (~26.6°), illite, and a little amount of hematite [Ihekweme et al., 2020; Adeniyi et al., 2020]. The presence of quartz adds thermal stability to membrane firing.

Burnt Rice Husk (BR h) in Figure 8[d] shows distinct changes compared to raw rice husk, with prominent Quartz (SiO_2) peaks indicating conversion to or retention of crystalline quartz structure. Other phases include Silica-Aluminate, Calcium Oxide, Ferrite, and Mullite. The appearance of new crystalline phases like mullite results from high-temperature treatment during combustion. Burning promotes amorphous silica crystallization to quartz/cristobalite/mullite, as in RHA studies where high temperatures yield these phases [Xu et al., 2012; Jonathan et al., 2020]. Mullite formation enhances pozzolanic activity and membrane strength. Burnt Clay (BCn) in Figure 4.10[e] reveals prominent Quartz (SiO_2) peaks alongside Iron Oxide (Fe_2O_3), Calcium Carbonate ($CaCO_3$), Aluminum Silicate ($AlSiO_4$), Calcium Silicate (Ca_2SiO_4), and Aluminum Hydroxide (Al (OH)). The burning process led to the formation or retention of specific crystalline minerals important for strength and durability in construction applications. Firing causes persistence of quartz, formation of mullite/hematite, and partial decomposition of clays/hydroxides (El Ouahabi et al., 2015). Quartz and iron oxides persist for durability. Snail Shell (Sn) in Figure 32 is dominated by intense Calcium Carbonate ($CaCO_3$) peaks, consistent with aragonite or calcite composition. Other phases include Quartz (SiO_2), Iron Oxide (Fe_2O_3), Aluminum Silicate ($AlSiO_4$), Calcium Silicate (Ca_2SiO_4), Aluminum Hydroxide (Al (OH)), and Muscovite. The dominance of calcium carbonate demonstrates its function as the basic building block of the shell of the snail. Snail shells consist predominantly of aragonite/calcite (main peaks ~26–33° 2θ) with very small quantities of quartz/contamination from the environment [Parveen et al., 2020; Podaralla et al., 2024]. $CaCO_3$ serves as a flux/sintering agent in membranes.

3.1.7 Thermal Behaviour Assessment through Thermogravimetric and Differential Thermal Analysis (TGA/DTA) of the Membrane Percusors

This section covers Thermal Analysis, focusing on Thermogravimetric Analysis (TGA) and Differential Thermal Analysis (DTA), applied to different materials. TGA tracks how a sample's weight changes with temperature or time, usually in a controlled environment, revealing details about thermal stability, decomposition, and composition. DTA measures the temperature difference between the sample and a reference material as temperature varies, identifying endothermic and exothermic events such as phase changes, decomposition, and oxidation. Together, these methods provide a thorough understanding of the thermal behavior of materials, including moisture loss, volatile component release, and organic matter breakdown. The data shown in the upcoming figures, including weight loss percentages and key temperatures, are essential for understanding the thermal properties and possible uses of these materials.

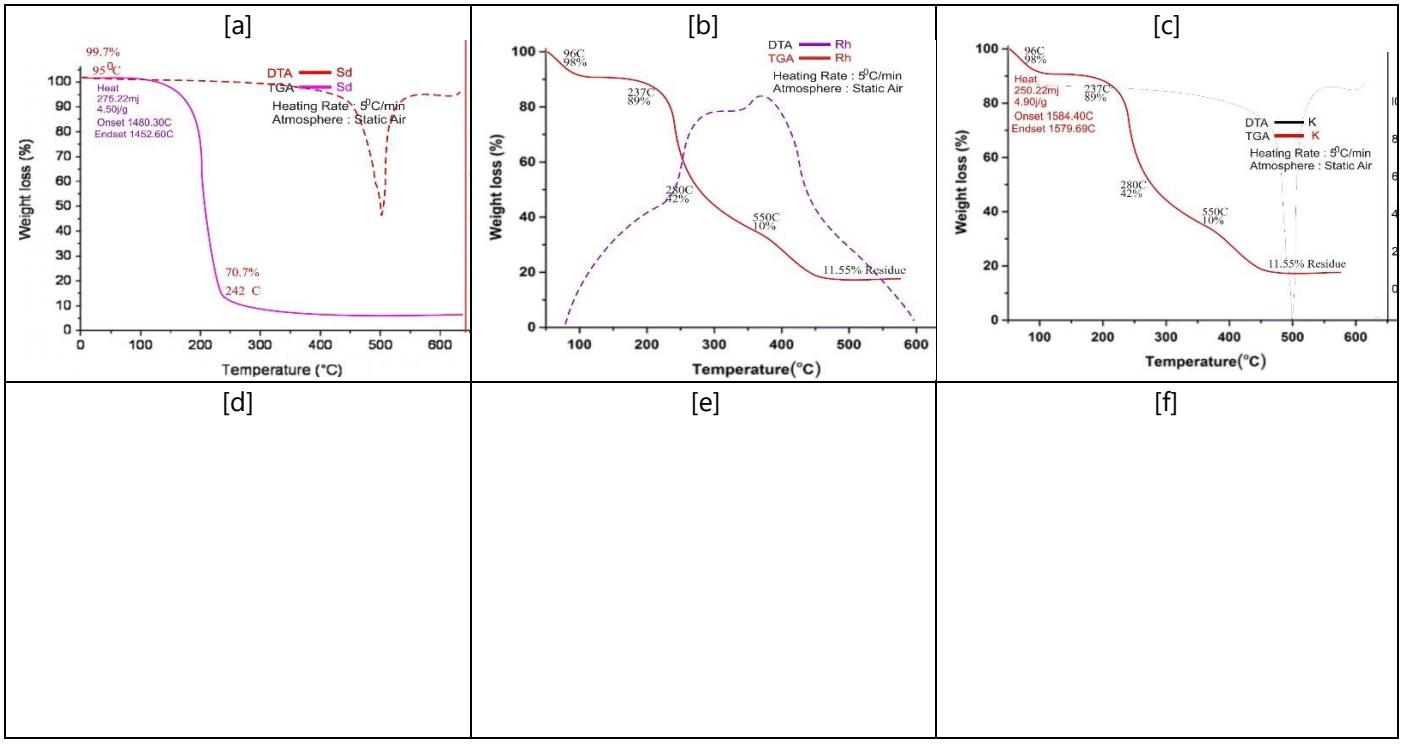

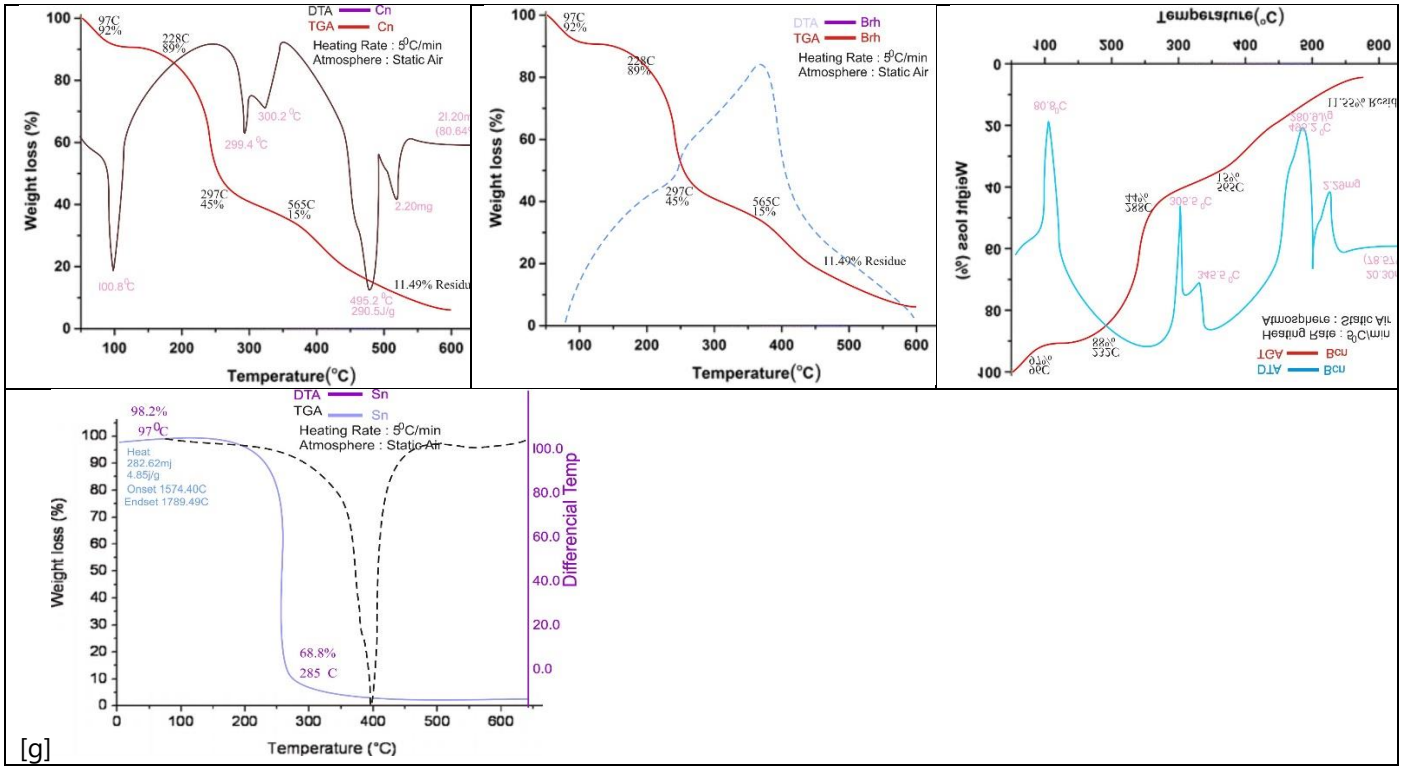

Figure 9: Thermogravimetric Analysis (TGA) and Differential Thermal Analysis (DTA) curves of ceramic membrane precursors. (a): Sawdust (Sd), (b): Rice Husk (Rh), (c): Kolin (K), (d): Clay (Cn), (e): Burnt Rice Husk (BRh), (j): Burnt Clay (BCn), (h): Snail Shell (Sn)

3.1.8 Discussion of the Thermal Behaviour Assessment through Thermogravimetric and Differential Thermal Analysis (TGA/DTA) of the Membrane Percusors

Sawdust (Sd) Thermal Analysis Figure 9[a] presents the TGA and DTA curves for Sawdust (Sd). The TGA curve shows significant weight loss occurring mainly in two stages. Initial slight weight loss around 95°C (99.7% remaining) is due to moisture evaporation. A major decomposition phase begins around 200°C, reaching 70.7% remaining at 242°C, characteristic of hemicellulose and cellulose degradation. The DTA curve shows an endothermic peak around 95°C corresponding to dehydration, followed by broad exothermic events indicating organic matter decomposition. Total heat measured is 275.22mJ (4.50J/g), with main degradation onset at 1480.30°C and endset at 1452.60°C. This aligns with wood/sawdust studies reporting two-stage decomposition (moisture <150°C, cellulose/lignin ~200–500°C) and exothermic peaks ~300–400°C [Jannat et al., 2021; Marques et al., 2025]. The high organic loss confirms its role as a pore former via burnout in sintering.

Rice Husk (Rh) Thermal Analysis. Figure 9[b] displays TGA and DTA curves for Rice Husk. Initial weight loss of about 2% up to 96°C is attributable to moisture removal. Significant degradation occurs from approximately 200°C to 400°C, with 89% remaining at 237°C, dropping to 42% at 280°C, and 10% at 550°C. This multi-stage decomposition reflects sequential degradation of hemicellulose, cellulose, and lignin. The DTA curve shows an endothermic peak associated with water loss, followed by a broad exothermic peak around 350-400°C, indicating combustion of organic components. Final residue at 600°C is approximately 11.55%, characteristic of rice husk silica content. This multi-stage pattern (hemicellulose → cellulose → lignin) and high silica residue match raw rice husk literature, where decomposition occurs ~220–550°C with ~15–20% ash (silica-rich) [Hossain et al., 2018; Serra et al., 2016]. The silica content supports its use as a pozzolanic additive in membranes.

Kaolin (K) Thermal Analysis. Figure 9[c] illustrates TGA and DTA curves for Kaolin. Initial weight loss of about 2% at 96°C corresponds to moisture removal. Main decomposition occurs in several stages, with 89% remaining at 237°C, 42% at 280°C, and 10% at 550°C. This multi-stage decomposition is typical for hydrated kaolin minerals, involving dehydroxylation of clay minerals. The DTA curve shows an endothermic peak at around 500°C, characteristic of kaolinite dehydroxylation. Total heat measured is 250.22mJ (70J/g), with decomposition onset at 1584.40°C and endset at 1579.69°C. Final residue at 600°C is 11.55%. This is typical for kaolinite, which loses ~14% water during dehydroxylation at ~450–600°C, forming metakaolinite (Ihekweme et al., 2020; Adeniyi et al., 2020). The residue (~11.55%) indicates partial silica/alumina stability.

Clay (Cn) Thermal Analysis. Figure 9[d] presents TGA and DTA curves for Clay. Initial weight loss of about 8% up to 97°C indicates moisture release. Subsequent weight losses occur at 228°C (89% remaining), 297°C (45% remaining), and 565°C (15% remaining), corresponding to organic matter decomposition and clay mineral dehydroxylation. The DTA curve exhibits several endothermic and exothermic peaks, with a notable endothermic peak at 100.8°C (21.20mg, 80.64% remaining) and another at 299.4°C. A significant endothermic peak at 495.2°C (290.5J/g) with weight loss of 2.20mg (11.49% residue) indicates major dehydroxylation of clay minerals. Final residue at 600°C is 11.49%. Final residue ~11.49%. This matches Nigerian clays with moisture loss <150°C and kaolinite/illite dehydroxylation ~450–600°C, often with organic combustion if contaminated [Ihekweme et al., 2020; [El Ouahabi et al., 2015].

Burnt Rice Husk (BR h) Thermal Analysis Figure 9[e] displays TGA and DTA curves for Burnt Rice Husk. Initial weight loss of approximately 8% up to 97°C is likely due to residual moisture. Further weight losses occur at 228°C (89% remaining), 297°C (45% remaining), and 565°C (15% remaining), indicating decomposition of remaining unburnt carbonaceous material or volatile organic compounds from incomplete combustion. The DTA curve shows broad exothermic events indicating oxidation of carbon residues. Final residue at 600°C is 11.49%, indicative of ash content, primarily silica. Post-burning RHA shows reduced organics, higher thermal stability, and minor exothermic oxidation of residual carbon [Jonathan et al., 2020; Xu et al., 2012].

Burnt Clay (BCn) Thermal Analysis. Figure 9[f] presents TGA and DTA curves for Burnt Clay. Initial weight loss of about 3% at 96°C corresponds to moisture evaporation. Subsequent weight losses observed at 232°C (88% remaining), 288°C (44% remaining), and 565°C (15% remaining) indicate decomposition of residual organic matter or dehydroxylation of partially converted clay minerals. The DTA curve exhibits multiple endothermic and exothermic peaks, with endothermic peaks at 80.8°C (20.30mg, 78.57% remaining) and 305.5°C. A prominent endothermic peak at 499.2°C (280.9J/g) with weight loss of 2.29mg (11.55% residue) corresponds to dehydroxylation of remaining clay phases not fully converted during burning. The final residue at 600°C is 11.55%. Residue ~11.55%. Firing diminishes dehydroxylation peaks (transformation to metakaolinite/mullite, partial), and the losses due to volatiles (organic material and clay minerals) are lower [El Ouahabi et al., 2015; Schackow et al., 2020], with the ends of volatiles or mineral phases causing small losses of material.

Snail Shell (Sn) Thermal Analysis Figure 9[g] displays TGA and DTA curves for Snail Shell. Initial minor weight loss of around 1.8% at 97°C is attributed to moisture. The most significant weight loss occurs abruptly between approximately 200°C and 400°C, with 68.8% remaining at 285°C. This major weight loss is characteristic of calcium carbonate ($CaCO_3$) decomposition into calcium oxide (CaO) and carbon dioxide (CO_2). The DTA curve shows a large endothermic peak around 350-400°C, consistent with the decarbonation process. Total heat measured is 282.62mJ (4.85J/g), with onset at 1574.40°C and end set at 1789.49°C. This matches snail shell studies where calcite/aragonite decomposes ~600–900°C (endothermic ~750–850°C in pure form), but lower temperatures occur in composites or impure samples [Parveen et al., 2020; Podaralla et al., 2024]. $CaCO_3$ decomposition provides fluxing and pore creation during sintering.

3.1.9 Results of the Functional Group Analysis Using Fourier Transform Infrared Spectroscopy (FTIR)

This section focuses on Molecular Spectroscopy, specifically Fourier Transform Infrared Spectroscopy (FTIR). FTIR is a technique used to obtain an infrared spectrum of absorption or emission of a solid, liquid, or gas. It identifies

functional groups and chemical bonds present in a molecule by measuring the absorption of infrared radiation at different wavelengths. When infrared light passes through a sample, certain frequencies are absorbed, corresponding to the vibrational modes of the chemical bonds within the sample. The resulting spectrum, plotted as transmittance or absorbance versus wavenumber (cm^{-1}), provides a unique chemical fingerprint of the material. This technique is invaluable for qualitative analysis of organic and inorganic compounds, helping to identify the presence of specific functional groups, characterize molecular structures, and assess changes in chemical composition due to treatment or reactions.

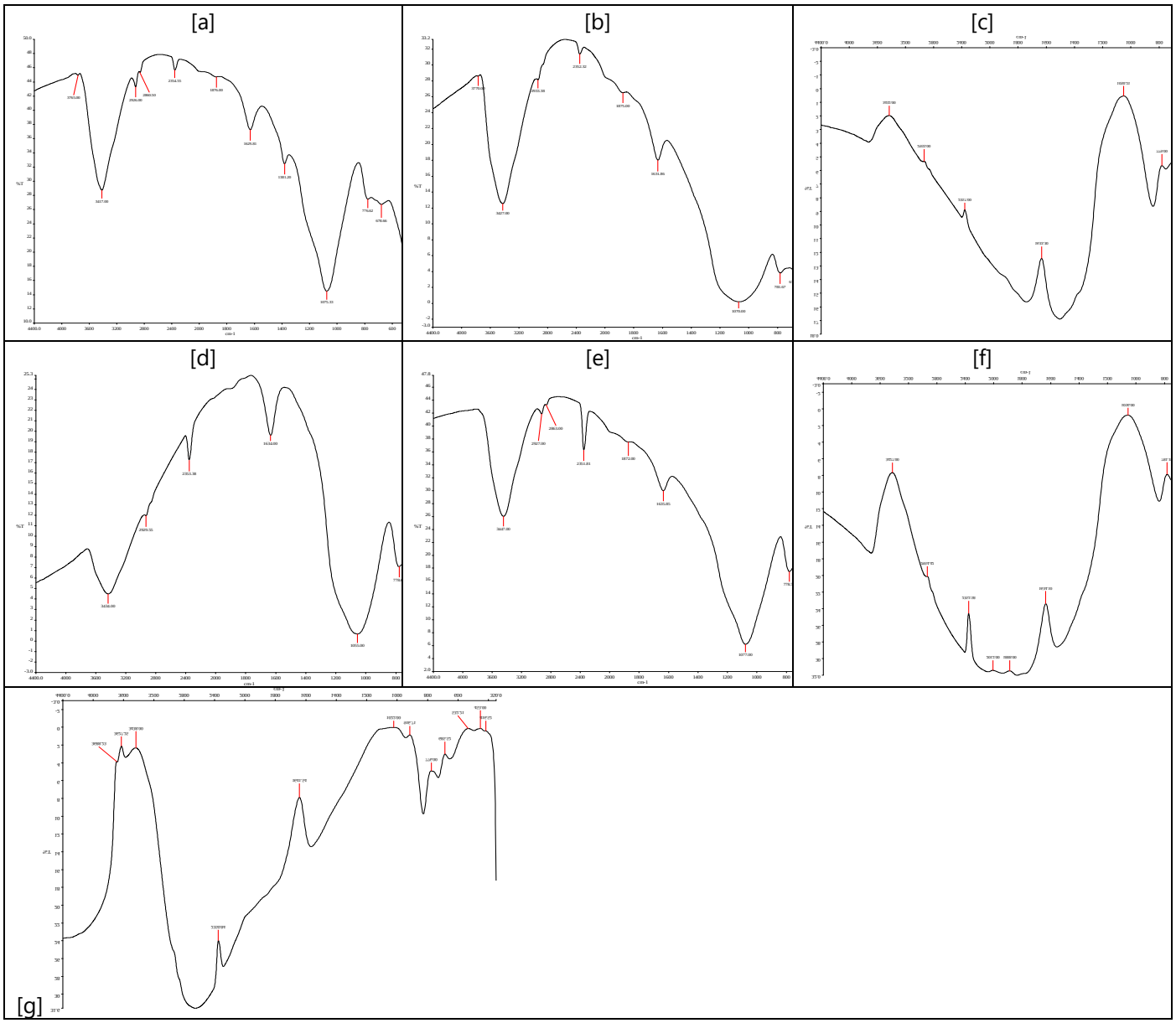

Figure 4.10: Functional Group Analysis curves of ceramic membrane precursors. (a): Sawdust (Sd), (b): Rice Husk (Rh), (c): Kolin (K), (d): Clay (Cn), (e): Burnt Rice Husk (BRh), (j): Burnt Clay (BCn), (h): Snail Shell (Sn)

3.1.10 Discussion of the Functional Group Analysis Results Using Fourier Transform Infrared Spectroscopy (FTIR)

Kaolin (K) FTIR Spectroscopy Figure 10[a] presents the FTIR spectrum for Kaolin, displaying characteristic absorption bands of kaolin clay. A broad band centered around 3600-3700 cm^{-1} indicates O-H stretching vibrations from

hydroxyl groups. A sharp peak around 1000 cm^{-1} corresponds to Si-O stretching vibrations, confirming the presence of silicates. Smaller peaks in the 900-750 cm^{-1} region are associated with Al-O-H bending vibrations. Absorption at approximately 500 cm^{-1} and 460 cm^{-1} can be assigned to Si-O-Si bending vibrations. The overall pattern is consistent with the known molecular structure of kaolinite. The pattern confirms kaolinite's layered aluminosilicate structure, matching that of Nigerian kaolin, where Si-O and OH dominate [Adeniyi et al., 2020].

Rice Husk (Rh) FTIR Spectroscopy Figure 10[b] exhibits absorption bands characteristic of lignocellulosic biomass and silica. A broad, strong band around 3300 cm^{-1} is attributed to O-H stretching from cellulose, hemicellulose, lignin, and adsorbed water. The band at approximately 2900 cm^{-1} corresponds to C-H stretching from aliphatic groups. A significant absorption band around 1050-1080 cm^{-1} is characteristic of Si-O-Si stretching, indicating high silica content. Peaks in the 1700-1600 cm^{-1} region relate to C=O stretching and adsorbed water. Smaller bands around 800 cm^{-1} and 470 cm^{-1} further support silica presence. This matches raw rice husk spectra: O-H ~3400 cm^{-1}, C-H ~2920 cm^{-1}, Si-O-Si ~1080 cm^{-1} (dominant silica), and C=O ~1730 cm^{-1} [Hossain et al., 2018; Jonathan et al., 2020]. High silica band confirms lignocellulosic-silica composition.

Burnt Rice Husk (BR h) FTIR Spectroscopy Figure 10[c] displays the spectrum for Burnt Rice Husk, showing significant changes due to burning. The O-H stretching band around 3400 cm^{-1} remains present, possibly from residual water or surface hydroxyl groups. However, C-H stretching bands around 2900 cm^{-1} are greatly diminished, indicating removal of most organic components. The dominant feature is a strong broad band around 1050-1100 cm^{-1}, characteristic of Si-O-Si stretching vibrations. Additional bands at 800 cm^{-1} and 470 cm^{-1} confirm silica presence. This spectrum confirms transformation into silica-rich ash. This reflects organic burnout and silica enrichment, typical of RHA: strong Si-O-Si ~1080–1100 cm^{-1}, weak/eliminated organic bands, confirming amorphous/crystalline silica post-combustion [Jonathan et al., 2020; Xu et al., 2012]. Changes indicate transformation to silica-rich ash for pozzolanic/membrane use.

Snail Shell (Sn) FTIR Spectroscopy Figure 10[d] is dominated by absorption bands characteristic of calcium carbonate. Strong broad bands around 1400 cm^{-1} and 870 cm^{-1} are assigned to asymmetric stretching and out-of-plane bending vibrations of carbonate ions. A smaller band around 712 cm^{-1} is also associated with carbonate. The broad O-H stretching band around 3400 cm^{-1} is likely due to adsorbed water. Absence of prominent Si-O or C-H bands emphasizes calcium carbonate as the major component, confirming the predominant inorganic composition. These confirm $CaCO_3$ (aragonite/calcite) dominance, matching snail shell spectra: ν_3 ~1400–1470 cm^{-1}, ν_2 ~870–875 cm^{-1}, ν_4 ~700–712 cm^{-1} (aragonite-specific ~700/713 cm^{-1}) [Parveen et al., 2020; Podaralla et al., 2024]. Minor Si-O absence emphasizes the inorganic $CaCO_3$ role as flux.

Burnt Clay (BCn) FTIR Spectroscopy Figure 10[e] shows changes compared to raw clay, reflecting thermal alteration. O-H stretching bands around 3600-3700 cm^{-1} may be reduced due to dehydroxylation during burning. However, prominent Si-O stretching bands around 1000 cm^{-1} remain strong, indicating persistence of silicate structures. Appearance of new bands may indicate formation of new mineral phases or structural rearrangements from high temperatures. The presence of carbonate bands might suggest residual calcium carbonate or re-carbonation after burning. This aligns with fired kaolin/clay: loss of OH bands post-dehydroxylation (~450–600°C), retention of Si-O ~1000–1100 cm^{-1}, and formation of metakaolinite/mullite features [El Ouahabi et al., 2015; Obada et al., 2017]. Residual carbonate may indicate re-carbonation.

Sawdust (Sd) FTIR Spectroscopy Figure 10[f] is characteristic of lignocellulosic materials. A broad absorption band around 3300 cm^{-1} corresponds to O-H stretching from hydroxyl groups in cellulose, hemicellulose, lignin, and adsorbed moisture. Bands around 2900 cm^{-1} are attributed to C-H stretching of methyl and methylene groups. Peaks in the 1700-1600 cm^{-1} region indicate C=O stretching and adsorbed water. The prominent band at approximately 1030-1050 cm^{-1} is due to C-O stretching vibrations in cellulose and hemicellulose. The spectrum confirms the organic nature of sawdust, comprising primarily cellulose, hemicellulose, and lignin. This is typical of lignocellulosic biomass: O-H ~3300–3400 cm^{-1}, C-H ~2900 cm^{-1}, C=O ~1730–1740 cm^{-1}, C-O ~1030–1160 cm^{-1} [Jannat et al., 2021; Marques et al., 2025]. Bands confirm organic nature as pore former.

3.2 Optimal Membrane Characterization

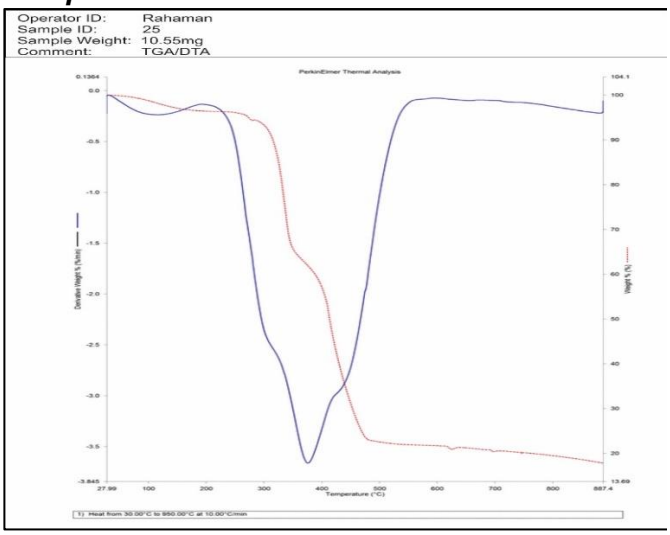

TGA/DTA

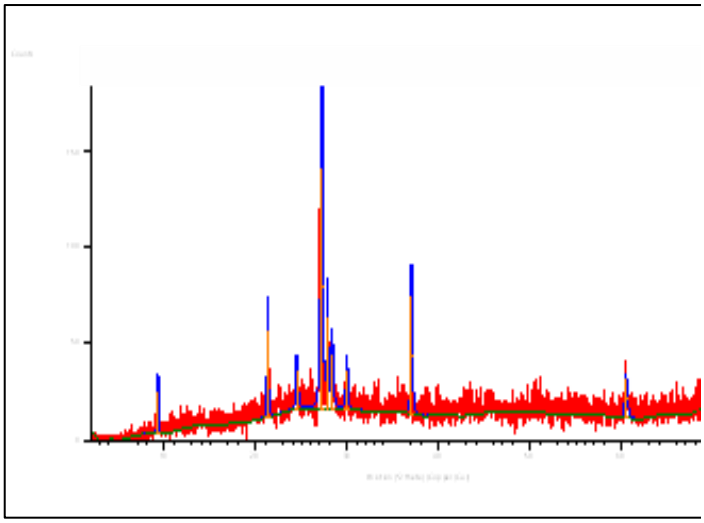

XRD

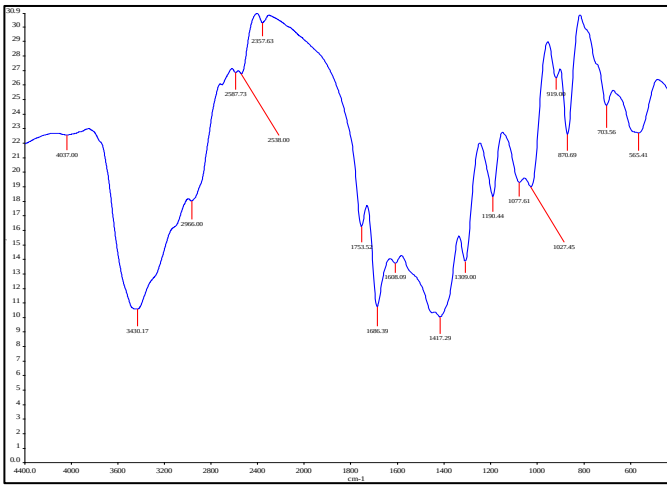

FITR

SEM

Figure 4.11: Optimal Membrane Characterisation Results [a] TGA/DTA, [b] XRD, [c] FITR, and [d] SEM

3.2.1 Discussion of the Results from the Optimal Membrane Characterization

The DTA/TGA curve for Sample 25 showcases its thermal nature at three separate stages in accordance with BET and XRD results. A slow weight loss at around 25°C to 150°C with an endothermic DTA dip denotes the loss of adsorbed water, attributed to the high surface area of the material. The sample is also stable with no apparent event between 150°Cand 400°C. Above 400°C, a sharp weight loss in the TGA and a sharp and large exothermic peak of the DTA take place, indicative of combustion of organics. Considering the XRD detection of zeolite and the BET surface area data, this event probably corresponds to the combustion of an organic template in synthetic zeolite production that leads to a porous structure, which results in the adsorptive property of the material.

The provided image represents the raw data extracted from an X-ray diffraction (XRD) analysis conducted on Sample 25, also designated as G-25. This measurement was performed using a copper X-ray source over a scanning range of 2° to 70° on the 2-theta scale, which is the standard range for identifying mineral phases. An additional data sheet listing the peaks showing where the X-rays intersected the planes of the crystal for the minerals detected is also provided. An important identifier of the sample is the most intense peak being located at 27.18° with a d-spacing measurement of 3.28 Å. The automated search and match routine performed using a database of minerals based on the obtained peak pattern resulted in the identification of the mineral species that were found. This raw

data file is the technical foundation that produced the earlier summary image showing minerals such as Quartz, Plagioclase, Biotite, and Zeolite, confirming that Sample 25 is a crystalline material with identifiable mineral phases.

The FTIR analysis confirms important chemical aspects of Sample 25, which is consistent with the XRD and TGA results. The peak at 3430 cm^{-1} is assigned to be the O-H stretching vibration of absorbed H_2O or a structurally hydroxyl group. A sharp peak at 2966 cm^{-1} shows the presence of C-H bonds, indicating organic residues, which is consistent with the TGA observations of combustion. The most intense band at 1077 cm^{-1} corresponds to the Si-O-Si asymmetric stretching vibration, further supporting the presence of a silicate framework as determined in the XRD analysis. Two more peaks at 703cm^{-1} and 565cm^{-1} were attributed to Si-O-Si symmetric stretching, and unique zeolite double ring vibrations confirmed the presence of microporous aluminosilicate material. The band at 1608 cm^{-1} is assigned to O–H bending of hydration. Overall, the spectrum identifies Sample 25 as a hydrated aluminosilicate with a zeolite-type structure containing organics, providing the explanation for the material's extremely high surface area and thermal properties.

This SEM reveals the surface morphology of the material, showing irregular grains, clusters, and visible voids. The coarse matrix is made of minute crystals and fine-grained or coarse-grained angular crystals (phenocrysts), with a porphyritic texture that is interconnected by pores. This aspect of the morphology is consistent with the BET surface area of 365 m^2/g and mean pore width of 24-25 Å, which indicates a hierarchical micro-mesoporous structure. The recognizable intergranular pores and cell spaces justify the capacity of this material to adsorb a great mass of materials, as the natural zeolite-clay-quartz aggregates in filtration applications.

3.2.2 X-Ray Fluorescence (XRF) Analysis

X-Ray Fluorescence analysis was conducted to determine the elemental composition of five clay samples. The results are presented as percentages for major element oxides and parts per million for trace elements.

Table 3: Major Element Composition (%)

Sample ID	SiO_2	Al_2O_3	Fe_2O_3	TiO_2	CaO	K_2O	MgO	Na_2O	LOI
Sample Cn	55.39	30.60	4.46	1.33	1.65	0.89	4.69	0.87	0.04
Sample Sd	56.26	29.22	75	1.25	1.55	0.98	4.75	0.90	0.02
Sample Sn	54.82	31.23	78	1.23	1.61	0.85	4.29	0.83	0.04
Sample Rh	58.50	28.42	2.26	1.23	1.46	6.01	2.06	0.89	0.05
Kaolin	60.30	28.52	1.65	1.25	1.50	0.96	4.70	0.95	0.02

Table 4: Trace Element Composition (ppm)

Sample ID	Ba	Cu	Cr	Ni	Zn	Co	Sr	Pb	Sc	Cd
Sample Cn	980.61	25.30	22.40	21.52	10.42	12.18	10.00	23.25	30.25	0.21
Sample Sd	894.60	24.21	28.20	10.40	40.45	11.30	42.11	20.30	8.15	0.08
Sample Sn	956.60	20.22	12.20	11.60	10.45	10.15	44.28	20.13	10.25	0.04
Sample Rh	882.30	24.30	33.20	15.60	45.25	13.15	32.10	20.20	8.45	0.12
Kaolin	890.50	20.18	26.40	10.44	32.48	13.20	32.41	5.30	8.20	0.06

The XRF results show that all the samples contain a high amount of silica (SiO_2) and alumina (Al_2O_3), ranging between 54.82 and 60.30 wt.% and 28.42 and 31.23 wt.%, respectively. This high silica, alumina content is typical of kaolinitic clay materials or aluminosilicate minerals. The Loss on Ignition is very low (0.02–0.05%), suggesting that there is little organic matter or carbonates. Sample Rh is distinctive with significantly higher potassium (6.01% K_2O) and lower iron and magnesium, pointing to a K-feldspar / illitic clay. Barium is the most prevalent trace element in all the samples, ranging from 882–980 ppm. The persistent presence of chromium, copper, and lead indicates a shared geological source, albeit with slight mineralogical variation.

3.2.3 Bet Surface Area Analysis

The data shows that Sample 25 has a BET surface area of 255.52 m^2/g, which means that it has a fairly large surface area that is typical of porous materials. Additionally, the very high correlation coefficient of 0.9996 demonstrates the reliability of the measurements. The t-Plot analysis indicates a micropore volume of 0.1556 cm^3/g with a micropore area of 55.28 m^2/g and an external surface area of 50.22 m^2/g. Significant differences found between the results of calculating a BET surface area and calculating the Langmuir surface area indicate that Sample 25 possesses microporous structures. The C-constant value calculated is 195.60, indicating theories favoring adsorption are supported by results from the tests performed on Sample 25, indicating that it is a porous material with both micropore and external surface areas, supporting the conclusion that the sample is suitable for adsorption-type applications.

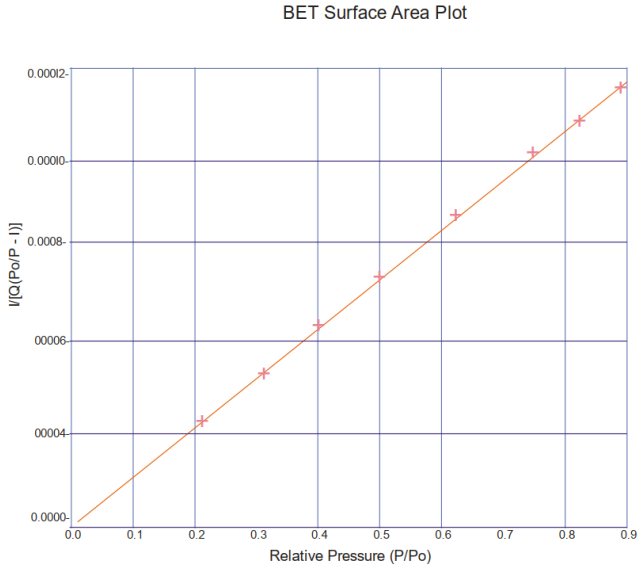

Figure 12: BET Surface Area Plot

4. Conclusion

This study successfully developed and comprehensively characterized an optimized low-cost multi-precursor ceramic membrane using locally sourced Nigerian agricultural and biogenic wastes (sawdust, rice husk, snail shell, kaolin, and natural clay). Through systematic pretreatment, homogeneous mixing with eco-friendly additives, uniaxial compaction, and precisely controlled sintering, flat-disk membranes with a functional top layer were fabricated at significantly lower cost than conventional commercial counterparts.

Detailed physicochemical analyses confirmed that the optimal membrane (Sample 25) possesses highly favorable properties for wastewater treatment applications: a BET surface area of 255.52 m^2/g with hierarchical micro-mesoporous architecture, crystalline phases (quartz, kaolinite, zeolite) that enhance structural integrity and adsorption capacity, porous and irregular surface morphology ideal for high flux and reduced fouling, and abundant surface functional groups (Si–O–Si, O–H) that facilitate electrostatic interactions and complexation. XRF data further validated the aluminosilicate-rich composition typical of effective ceramic matrices, while TG-DTA demonstrated excellent thermal stability across the fabrication temperature range.

These attributes enable synergistic removal of heavy metals (e.g., Pb (II), Cd (II)) and azo dyes (e.g., Disperse Yellow 7, Trypan Blue) via complementary mechanisms of size exclusion, adsorption, ion exchange, and Donnan exclusion. Integration of the membrane into a custom-designed stainless-steel treatment unit underscores its practical scalability for real-world industrial effluents. By valorizing abundant local wastes, the process advances circular-economy principles, drastically lowers material and energy costs, and addresses key barriers to widespread adoption of ceramic membrane technology in resource-limited settings.

The findings contribute meaningfully to sustainable water remediation and support UN Sustainable Development Goals 6 (clean water and sanitation) and 12 (responsible consumption and production). Future work will focus on pilot-scale performance evaluation with real industrial wastewater, long-term fouling behavior and regeneration studies, antifouling modifications (e.g., photocatalytic coatings), and machine-learning-assisted process optimization to facilitate commercialization. This research establishes a robust, reproducible platform for next-generation, affordable ceramic membranes tailored to the unique challenges of emerging economies.

ORCID:
[1]ORCID: 0000-0001-5819-9911, [2]ORCID: 0000-0001-6181-3150

References

[1] Adeniyi, F. I., Ogundiran, M. B., Hemalatha, T., & Hanumantrai, B. B. (2020). Characterization of raw and thermally treated Nigerian kaolinite-containing clays using instrumental techniques. SN Applied Sciences, *2*(5), 821. https://doi.org/10.1007/s42452-020-2610-x

[2] Akoumeh, R., Al-Ejji, M., Aljaoni, B and Abbas, M. (2025). Advances in ceramic membrane technology: Versatility of fabrication technique, industrial applications, and challenges, *Inorg. Chem. Commun.*, vol. 179. 114685, doi: 10.1016/j.inoche.2025.114685.

[3] Abhisek, K., Vhatkar, S.S., Mathew, H.T., Singh P and Oraon, R. (2025). A critical review on the challenges and techno-economic assessment of dyes removal technologies from wastewater, *Discov. Chem.*, 2(1). 1–37, doi: 10.1007/s44371-025-00111-4.

[4] Abu-Dief, A.M., Alsaedi W.H and Zikry M.M. (2025). A collective study on the fabrication of nano-materials for water treatment, *J. Umm Al-Qura Univ. Appl. Sci.*, doi: 10.1007/s43994-025-00227-4.

[5] Boussemghoune, A., Chihi, S., & Benmounah, A. (2020). Microstructural and mechanical properties of fired clay bricks incorporating natural waste materials. Journal of Building Engineering, *32*, 101–112.

[6] Bensalah, H., Derouich, G., Wang, X., Alami Younssi S and Bekheet, M.F. (2023). Graphene-Oxide-Grafted Natural Phosphate Support as a Low-Cost Ceramic Membrane for the Removal of Anionic Dyes from Simulated Textile Effluent, *Membranes*, 13(3). 345, doi: 10.3390/membranes13030345.

[7] El Ouahabi, M., Daoudi, L., Hatert, F., & Fagel, N. (2015). Modified mineral phases during clay ceramic firing. Clays and Clay Minerals, *63*(5), 404–413. https://doi.org/10.1346/CCMN.2015.0630506

[8] Hossain, S. S., Mathur, L., & Roy, P. K. (2018). Rice husk/rice husk ash as an alternative source of silica in ceramics: A review. Journal of Asian Ceramic Societies, *6*(4), 299–313. https://doi.org/10.1080/21870764.2018.1539210

[9] Ihekweme, G. O., Shondo, J. N., Orisekeh, K. I., Kalu-Uka, G. M., Nwuzor, I. C., & Onwualu, A. P. (2020). Characterization of certain Nigerian clay minerals for water purification and other industrial applications. Heliyon, *6*(4), e03783. https://doi.org/10.1016/j.heliyon.2020.e03783

[10] Jannat, N., Latif Al-Mufti, R., Hussien, A., Abdullah, B., & Cotgrave, A. (2021). Influence of sawdust particle sizes on the physico-mechanical properties of unfired clay blocks. Designs, *5*(3), 57. https://doi.org/10.3390/designs5030057

[11] Jarrar, R., Abbas M.K.G and Al-Ejji, M. (2024). Environmental remediation and the efficacy of ceramic membranes in wastewater treatment—a review, *Emergent Mater.*, 7(4). 1295–1327, Aug. 2024, doi: 10.1007/s42247-024-00687-0.

[12] Jonathan, K. M., Kuria, K. P., Mwangi, G. J., & Gichuki, N. F. (2020). Characterization of rice husk ash prepared by open air burning and furnace calcination. Journal of Chemical Engineering and Materials Science, *11*(2), 21–30. https://doi.org/10.5897/JCEMS2020.0348

[13] Kirk, C.H., Wang, P., Chong, C.Y.D., Zhao, Q., Sun J and Wang, J., (2024). TiO2 photocatalytic ceramic membranes for water and wastewater treatment: Technical readiness and pathway ahead, *J. Mater. Sci. Technol.* 152–164, June, doi: 10.1016/j.jmst.2023.09.055.

[14] Marques, A. V. S., Barbosa, A. dos S., Maia, L. F., Rodrigues, M. G. F., Lins Almeida Barbosa, T., & Luna, C. B. B. (2025). Development and characterization of sawdust-based ceramic membranes for textile effluent treatment. Membranes, *15*(10), 298. https://doi.org/10.3390/membranes15100298

[15] Malebadi, K.A., Sawunyama, L., Seheri N.H and Onwudiwe, D.C. (2025). Application of Ceramic Membranes Derived from Waste and Natural Materials for the Removal of Organic Dyes from Wastewater: A Review, *Ceramics*, 8(3). 80, doi: 10.3390/ceramics8030080.

[16] Mgbemere, H., Ekpe, I., Lawal, G., Ovri, H., & Chaudhary, A.-L. (2019). Preparation and characterization of zeolite type 4A using kaolin from Ajebo, Nigeria. Pertanika Journal of Science and Technology, *27*(4), 1865–1878.

[17] Mohamed Ariff, A. H., Othman, M. H. D., Tai, Z. S., Hubadillah, S. K., & Ismail, A. F. (2022). Rice husk-derived silica-based ceramic membranes for water treatment: A review. Journal of the European Ceramic Society, *42*(5), 1893–1912.

[18] Obada, D. O., Dodoo-Arhin, D., Dauda, M., Anafi, F. O., Ahmed, A. S., & Ajayi, O. A. (2017). The impact of kaolin dehydroxylation on the porosity and mechanical integrity of kaolin-based ceramics using different pore formers. Results in Physics, *7*, 2718–2727. https://doi.org/10.1016/j.rinp.2017.07.048

[19] Olorunnisola C.G. (2025). Clay-based photocatalytic membranes: low-cost alternative materials for water treatment," *Mater. Adv.*, 6(14). 4623–4645, 2025, doi: 10.1039/D5MA00313J.

[20] Onyenanu C.N and Nwabanne, J.T. (2025) Application of Ceramic Membranes for the Removal of Heavy Metals and Dyes: Efficiency and Performance Review, *Res. J. Civ. Ind. Mech. Eng.*, vol. 2, no. 2, pp. 84–98, 2025, doi: DOI:2010.61424/rjcime.v2i2.338.

[21] Oshani, F., Kargari, A., Norouzbeigi, R., & Mahmoodi, N. M. (2025). Performance optimization and fouling study of geopolymer-zeolite composite membranes for sustainable textile wastewater treatment. Scientific Reports, *15*(1), 35463. https://doi.org/10.1038/s41598-025-19349-0

[22] Onyenanu C.N and Onyenanu, I.U. (2025). Advanced Treatment Technologies for Heavy Metal Removal from Water and Wastewater: A Comprehensive Review, IJANS, vol. 3, no. 2, pp. 111–131, Jun. 2025.

[23] Parveen, S., Chakraborty, A., Chanda, D. K., Pramanik, S., Barik, A., & Aditya, G. (2020). Microstructure analysis and chemical and mechanical characterization of the shells of three freshwater snails. ACS Omega, *5*(40), 25757–25771. https://doi.org/10.1021/acsomega.0c03064

[24] Podaralla, N. K., Paramasivam, P., & Jacquemin, J. (2024). Characterization of hydrothermally decomposed and synthesized $CaCO_3$ reinforcement from dead snail shells. ACS Omega, *9*(2), 2183–2191. https://doi.org/10.1021/acsomega.3c05330

[25] Prabhakar, N., Isloor, A.M., Farnood R and Ismail, A.F. (2025). Efficient removal of hazardous dyes/heavy-metal ions by in-house fabricated poly (vinylidene fluoride) thin-film nanocomposite membranes with functionalized Zr-based metal-organic framework, *J. Environ. Chem. Eng.*, vol. 13, no. 3, p. 116434, doi: 10.1016/j.jece.2025.116434.

[26] Ramanamane, K. P., Kaseka, P. K., & Nkosi, S. S. (2024). Hierarchical mesoporous materials from clay and rice husk for wastewater treatment applications. Journal of Porous Materials, *31*(3), 789–802.

[27] Rakcho Y *et al.* (2025). Fabrication of low-cost ceramic nanofiltration membrane from natural resources for the removal of cationic and anionic dyes: Experimental and DFT investigations, *Chem. Eng. J.* 159779, doi: 10.1016/j.cej.2025.159779.

[28] Schackow, A., Stringari, D., Senff, L., Correia, S. L., & Segadães, A. M. (2020). Influence of firing temperature on the physical and mechanical properties of red ceramic. Ceramics International, *46*(10), 15678–15685.

[29] Santra, B., Ramrakhiani, L., Kar, S. Ghosh, S and Majumdar, S. (2020). Ceramic membrane-based ultrafiltration combined with adsorption by waste-derived biochar for textile effluent treatment and management of spent biochar, *J. Environ. Health Sci. Eng.*, 18(2). 973–992, doi: 10.1007/s40201-020-00520-w.

[30] Sandhya Rani S.L and Kumar, R.V. (2021). Insights on applications of low-cost ceramic membranes in wastewater treatment: A mini-review, *Case Stud. Chem. Environ. Eng.*, p. 100149, Dec., doi: 10.1016/j.cscee.2021.100149.

[31] Sawunyama, L., Olatunde, O.C., Oyewo, O.A., Bopape, M.F and Onwudiwe, D.C. (2024). Application of coal fly ash-based ceramic membranes in wastewater treatment: A sustainable alternative to commercial materials," *Heliyon*, vol. 10, no. 2, p. e24344, Jan. 2024, doi: 10.1016/j.heliyon. 2024.e24344.

[32] Solaiman, J.M., Rajamohan, N., Yusuf M and Kamyab, H. (2024). Nanocomposite ceramic membranes as novel tools for remediation of textile dye waste water – A review of current applications, machine learning based modeling and future perspectives," *J. Environ. Chem. Eng.*, vol. 12(2) 112353, doi: 10.1016/j.jece.2024.112353.

[33] Serra, M. F., Conconi, M. S., Gauna, M. R., Suárez, G., Aglietti, E. F., & Rendtorff, N. M. (2016). Mullite ($3Al_2O_3{\cdot}2SiO_2$) ceramics obtained by reaction sintering of rice husk ash and alumina, phase evolution, sintering, and microstructure. Journal of Asian Ceramic Societies, *4*(1), 61–67. https://doi.org/10.1016/j.jascer.2015.11.003

[34] Thiedeitz, M., Schmidt, W., & Härder, M. (2020). Rice husk ash as a sustainable pozzolan in concrete: A review. Construction and Building Materials, *263*, 120–132.

[35] Tripathi M *et al. (2023).* Recent Strategies for the Remediation of Textile Dyes from Wastewater: A Systematic Review, *Toxics*, 11(11). 940, doi: 10.3390/toxics11110940.

[36] Tayara, A., Shang, C., Zhao J and Xiang, Y. (2024). Machine learning models for predicting the rejection of organic pollutants by forward osmosis and reverse osmosis membranes and unveiling the rejection mechanisms, *Water Res.*, 266. 122363, doi: 10.1016/j.watres.2024.122363.

[37] Velusamy, S., Roy, A., Sundaram S and Kumar Mallick T. (2021) A Review on Heavy Metal Ions and Containing Dyes Removal Through Graphene Oxide-Based Adsorption Strategies for Textile Wastewater Treatment, *Chem. Rec.*, 21(7). 1570–1610, 2021, doi: 10.1002/tcr. 202000153.

[38] Wang, X., Wang, M. Chen M and Zhang, Y. (2023). A Mini Review of Ceramic-Based MOF Membranes for Water Treatment, *Membranes*, 13(9). 751, doi: 10.3390/membranes13090751.

[39] Xu, W., Lo, T. Y., & Memon, S. A. (2012). Microstructure and reactivity of rich husk ash. Construction and Building Materials, *29*, 541–547. https://doi.org/10.1016/j.conbuildmat.2011.11.005

[40] Yang, Y., Wang, L., & Zhang, J. (2023). Morphological characterization of kaolinite using SEM and AFM techniques. Applied Clay Science, *235*, 106–118.
[41] Ye Y *et al.* (2025). Integrating artificial intelligence with mechanistic epidemiological modeling: a scoping review of opportunities and challenges, *Nat. Commun.*, 16(581), doi: 10.1038/s41467-024-55461-x.
[42] Yepes, J. L., Torres, A., & Muñoz, F. (2011). Morphological characterization of wood dust particles. Wood Science and Technology, *45*(4), 621–634.